CONDENSED MATTER PHYSICS

Strain-switchable field-induced superconductivity

Joshua J. Sanchez[1,2]*, Gilberto Fabbris[3], Yongseong Choi[3], Jonathan M. DeStefano[2], Elliott Rosenberg[2], Yue Shi[2], Paul Malinowski[2,4], Yina Huang[5], Igor I. Mazin[6], Jong-Woo Kim[3], Jiun-Haw Chu[2]*, Philip J. Ryan[3]*

Field-induced superconductivity is a rare phenomenon where an applied magnetic field enhances or induces superconductivity. Here, we use applied stress as a control switch between a field-tunable superconducting state and a robust non–field-tunable state. This marks the first demonstration of a strain-tunable superconducting spin valve with infinite magnetoresistance. We combine tunable uniaxial stress and applied magnetic field on the ferromagnetic superconductor $Eu(Fe_{0.88}Co_{0.12})_2As_2$ to shift the field-induced zero-resistance temperature between 4 K and a record-high value of 10 K. We use x-ray diffraction and spectroscopy measurements under stress and field to reveal that strain tuning of the nematic order and field tuning of the ferromagnetism act as independent control parameters of the superconductivity. Combining comprehensive measurements with DFT calculations, we propose that field-induced superconductivity arises from a novel mechanism, namely, the uniquely dominant effect of the Eu dipolar field when the exchange field splitting is nearly zero.

INTRODUCTION

Switching between distinct electronic phases in quantum materials by external tuning parameters is a central focus of condensed matter physics, both to study how competing orders interact and to drive technological development (*1*). One rich research area is tuning systems with both ferromagnetism and superconductivity. The interaction of these antagonistic phases leads to unusual phenomena, such as spontaneous magnetic vortices (*2*–*4*) and spin-polarized supercurrents (*5*–*7*), which hold promise for superconducting spintronics technologies and energy-efficient data storage. Much attention has focused on superconducting spin valves, i.e., heterostructures with ferromagnetic layers surrounding a superconducting layer (*5*–*8*). An applied magnetic field switches the sandwiching ferromagnetic layers between parallel and antiparallel alignment, which strongly tunes the magnetic pairbreaking effect and effectively turns the superconductivity on and off. This enables the ultimate switchability of magneto-transport, between a resistive and zero-resistance state, thus achieving infinite magnetoresistance and the possibility of low-energy dissipation information technologies (*5*).

The development of these technologies is impeded by the very low temperatures required to implement them. Besides artificial heterostructures, a handful of single-crystal materials exhibit field-induced superconductivity, including several Eu- and U-based superconductors (*9*–*14*) and organic superconductors (*15*, *16*). In these systems as well as in thin-film superconducting spin valves, the zero-resistance temperature T_0 is often below 1 K, limiting their practical application. The current highest field-induced superconductivity temperature is in the chemically doped Eu-based iron pnictide superconductor, $EuFe_2As_2$. Like other iron pnictide superconductors, $EuFe_2As_2$ exhibits an electronic nematic transition, which creates orthorhombic structural twin domains. The suppression of nematicity by chemical doping results in the emergence of both superconductivity, with an onset temperature T_{SC} reaching 18 to 30 K at optimal doping (*17*–*22*), and Eu ferromagnetism, with T_{FM} = 16 to 20 K (*2*, *23*–*26*). The similar ordering temperatures of the two antagonistic phases implies a potentially strong competition between them. For Co- and Rh-doped samples, a large reentrant resistivity appears below T_{FM} as the Eu magnetic flux disrupts the nascent superconductivity, pushing T_0 far below T_{SC}. Unexpectedly, applying a small in-plane magnetic field ($\mu_0 H < 0.5$ T) to these materials raises T_0 from ~5 K to ~6 to 7 K (*27*, *28*). To date, the underlying mechanism of this field-induced superconductivity has not been determined, nor has the effect been optimized to enhance T_0 to its limit.

Here, we demonstrate field-induced superconductivity in 12% Co-doped $EuFe_2As_2$ at T_0 = 9 K, which can be enhanced up to at least 10 K or suppressed to 4 K using in situ applied uniaxial stress. To our knowledge, this is the highest reported temperature of magnetic field–induced superconductivity in any material. Doped $EuFe_2As_2$ exists as a natural-grown atomic limit of the thin-film superconducting spin valve architecture, with alternating ferromagnetic Eu and superconducting/nematic FeAs layers (Fig. 1A). We combine synchrotron x-ray techniques with transport measurements to reveal that strain tuning nematicity and field tuning the Eu moments act as independent superconductivity control parameters (Fig. 1, B and C). This strain tunability, combined with the high temperature and low switching field, makes doped $EuFe_2As_2$ an exciting platform for potential superconducting spintronics applications, and we propose a new superconducting switch device concept using this strain tunability.

Finally, we perform density functional theory (DFT) calculations to show that the cancellation of Eu-Fe ferromagnetic and antiferromagnetic exchange interactions results in a very weak exchange field, which solves the mystery of how the superconducting order can coexist with ferromagnetism. In the near absence of the exchange field, the Eu dipole field has a dominant effect on the

[1]Department of Physics, Massachusetts Institute of Technology, Cambridge, MA 02139, USA. [2]Department of Physics, University of Washington, Seattle, WA 98195, USA. [3]Advanced Photon Source, Argonne National Laboratory, Lemont, IL 60439, USA. [4]Department of Physics, Cornell University, Ithaca, NY 14853, USA. [5]Department of Physics, Zhejiang University of Science and Technology, Hangzhou 310023, People's Republic of China. [6]Department of Physics and Astronomy and Quantum Science and Engineering Center, George Mason University, Fairfax, VA 22030, USA.
*Corresponding author. Email: sanchezx@mit.edu (J.J.S.); jhchu@uw.edu (J.-H.C.); pryan@anl.gov (P.J.R.)

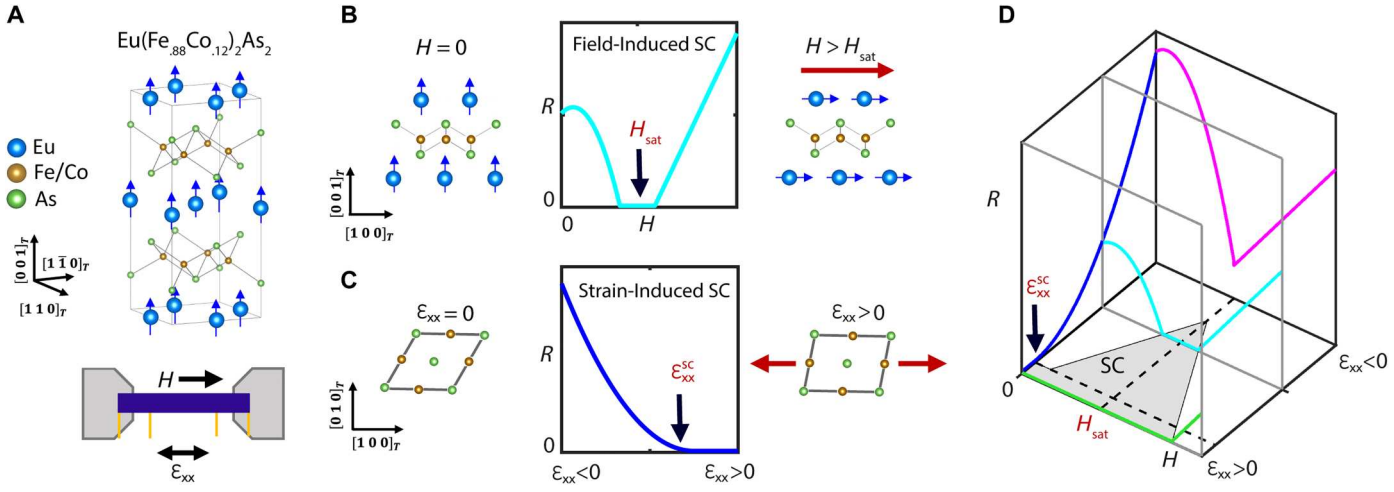

Fig. 1. Strain and field-tunable ferromagnetic superconductivity. (**A**) $Eu(Fe_{.88}Co_{.12})_2As_2$ consists of stacked planes of Eu and doped FeAs layers, with the former exhibiting ferromagnetism (FM; T_{FM} = 17 K) and the latter hosting both nematicity (N; T_S = 68 K) and superconductivity (SC; T_{SC} = 19 K). Below T_{FM}, the coexistence and competition between the three phases enables exceptional tunability of the superconductivity. (**B**) A small in-plane magnetic field reorients the Eu moments from out of plane to in plane, reducing the magnetic flux through the FeAs layers. A zero-resistance (R = 0) state occurs in the vicinity of the full saturation of the moments in plane (at $H = H_{sat}$), demonstrating field-induced superconductivity. (**C**) As in other iron-pnictide superconductors, the N/SC phase competition enables an effective strain tuning of superconductivity via strain tuning the lattice-coupled nematic order. Tensile strain ($\varepsilon_{xx} > 0$) along the FeAs bonding direction suppresses the nematicity-driven orthorhombicity along the FeFe bonding direction. This enhances superconductivity, with the entrance into the R = 0 state labeled as ε_{xx}^{sc}. (**D**) Combined strain and field tuning of the resistivity defines an R = 0 superconducting region of the phase diagram (gray) at one fixed temperature, with a precise shape that depends on the (temperature-dependent) values of ε_{xx}^{sc} and H_{sat}. For fields from H = 0 to $H = H_{sat}$, strain selects between an always metallic state (magenta), an always superconducting state (green), and a field-induced superconducting state (cyan). Thus, strain acts like a toggle switch for the phase field tunability.

superconductivity. We introduce a new mechanism for field-induced superconductivity, whereby an external field reorients this internal dipole field from the direction of lower to higher upper critical field H_{c2}, enabling the applied field to enhance T_0. We consider how this novel mechanism could be realized in other systems, including in two-dimensional (2D) systems and at even higher temperatures.

RESULTS

Strain-switchable field-induced superconductivity

Single-crystal samples of 12% Co-doped $EuFe_2As_2$ were grown using Sn flux (see Materials and Methods). Using a (Fe,Co)–rich, nonstoichiometric growth composition yielded samples with increased superconducting transition temperatures relative to stoichiometric-grown samples (Materials and Methods and fig. S1) (*27*). Samples 1 and 2 were selected from different growth batches and were prepared identically as matchsticks to measure the inline resistivity ρ_{xx} (Fig. 1A, bottom). To better compare the field and strain tuning of the resistivity, transport data are normalized to the zero-field freestanding resistivity at T = 25 K, with $\rho/\rho_0 = \rho_{xx}(T, \mu_0 H, \varepsilon_{xx})/\rho_{xx}(25\text{ K},0,0)$.

In the freestanding state, sample 1 was cooled through the superconducting (T_{SC} = 19 K, onset temperature at ρ/ρ_0 = 0.99) and ferromagnetic (T_{FM} = 17.2 K, at the minimum of ρ/ρ_0) transitions under zero field (Fig. 2, black), reaching ρ/ρ_0= 0 at T_0 = 7.5 K. Temperature sweeps were repeated with fixed magnetic field applied either in plane (Fig. 2, red) or out of plane (Fig. 2, blue). The latter is found to increase the resistivity and reduce the value of T_0. In sharp contrast, an in-plane field is far more detrimental to superconductivity between T_{SC} and T_{FM}, but zero resistance is reached at an enhanced value of T_0 = 9.0 K for $\mu_0 H$ = 0.2 T, thus demonstrating field-induced superconductivity.

Figure 3A shows ρ/ρ_0 versus temperature at fixed in-plane field ($\mu_0 H$ = 0 T and $\mu_0 H$ = 1 T) and ρ/ρ_0 versus field at fixed temperature for sample 1. For $T > T_{FM}$, an applied field up to 1 T acts only to increase the resistivity. For $T < T_0$, ρ/ρ_0 = 0 up to 1 T. However, for $T_{FM} > T > T_0$, the minimum resistivity value is reached at finite field. As we will show, this resistivity minimum corresponds to the full in-plane saturation of the Eu moments, and we mark this field value as H_{sat} (Fig. 3B, black circles). Figure 4 presents H_{sat} versus temperature, which follows a square root temperature dependence, $H_{sat} \propto \sqrt{T_{FM} - T}$, indicating the mean-field behavior of the Eu magnetic ordering. For 9 K > T > 7.5 K, zero resistance can be induced in the vicinity of H_{sat}.

Following these measurements, sample 1 was mounted to a uniaxial stress device (see Materials and Methods and figs. S6 and S7). Stress was applied along the Fe-As bonding direction, inducing strain in both B_{1g} and A_{1g} symmetry channels. The sample was initially cooled under zero device voltage to base temperature and then was slowly warmed under large fixed tension or compression to yield the resistivity versus temperature curves in Fig. 4 (right). We find that T_{SC} varies monotonically with strain and is tuned by ~1 K, revealing the tunability of the nematicity/superconductivity phase competition in line with previous work in $BaFe_2As_2$ (*29*, *30*). Below T_{FM}, the resistivity is especially tunable, and T_0 is tuned by ~3 K (and fully suppressed under maximum compression; see fig. S6). However, the Eu magnetic order is apparently independent of strain, as T_{FM} is constant across this strain range.

Applying field at fixed temperature and stress (Fig. 3C) enables the construction of a superconductivity strain field-tunable phase diagram (Fig. 4). Field-induced superconductivity is accessible in

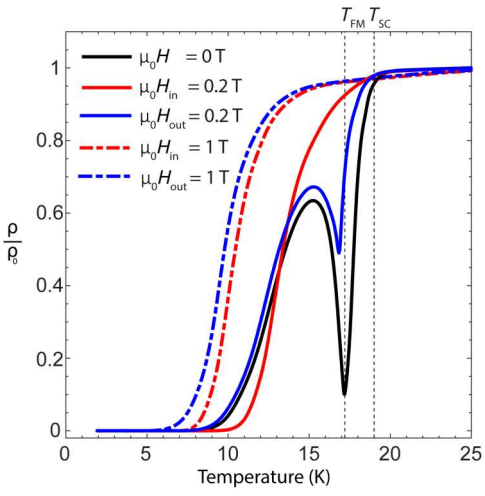

Fig. 2. Zero-strain field-induced superconductivity. Sample 1 resistivity versus temperature for zero applied field (black) and μ_0H = 0.2 T (solid line) and 1 T (dashed line) applied in plane (red) and out of plane (blue). For μ_0H = 0.2 T applied in plane, the zero-resistivity temperature rises from T_0 = 7.5 to 9.0 K.

a temperature window from 7.5 to 9 K under zero strain, with a maximum near 11 K under tension and a minimum of 4 K under compression. With decreasing temperature, an increasing Eu magnetic moment causes the ferromagnetism to have a larger influence on the superconductivity, and so the zero-resistance phase volume increases under compression and decreases under tension. Across this range, the onset field only varies between μ_0H = 0.1 T and 0.3 T; we note that this is a substantial qualitative difference from UTe_2 where pressure tuning can shift the critical field by many tesla (*14*).

Strain and magnetic field: Independent tuning knobs of superconductivity

To further identify the independence of strain and magnetic field for tuning superconductivity, as well as to resolve the mechanism of the field-induced superconductivity, we performed transport measurements under applied strain concurrent with either x-ray diffraction (XRD) or x-ray magnetic circular dichroism (XMCD) at the Advanced Photon Source. XMCD is a powerful tool to study ferromagnetic superconductors. It provides element-specific magnetic information, and, carried out in fluorescence mode, any diamagnetic shielding from the superconductivity is avoided.

We performed XRD measurements on sample 2 at T = 13.5 K, just below the maximum of the reentrant resistivity, across a range of strain. The linearity of the inline strain ε_{xx} confirms a constant strain transmission (Fig. 5B). We also measured the B_{2g}-symmetry spontaneous orthorhombicity ε_S, which is a proxy of the nematic order (see Materials and Methods and fig. S2) (*31*). Under applied tension, the magnitude of ε_S is suppressed by up to 30%, coinciding with a dramatic decrease in the resistivity (Fig. 5A). Under compression, ε_S is roughly constant as the resistivity increases, suggesting that the saturated nematicity suppresses the superconductivity. This strain dependence of nematicity is consistent with the combination effect of the induced A_{1g} and B_{1g} strains, where the latter acts as a transverse field that suppresses nematicity quadratically. Thus, we effectively strain-tune superconductivity via its competition with the strain-tunable nematicity and the associated antiferromagnetic order (*30*, *32*).

Field-induced superconductivity was observed at T = 10 K under both fixed-strain and fixed-field conditions. With zero field, the resistivity can be strain-tuned from ρ/ρ_0 = 5% under zero strain, to ρ/ρ_0 = 40% at maximum compression, and ρ/ρ_0 = 0% with maximum tension (Fig. 5C). Thus, tensile strain can effectively raise the superconducting transition to at least 10 K. The application of an in-plane magnetic field (μ_0H = 0.26 T) decreases the resistivity at all strain states, and zero resistivity is obtained at roughly 75% of the maximum applied tension. Thus, tensile strain and magnetic field can work together to raise the transition temperature even higher. Figure 5D shows resistivity versus applied magnetic field at four fixed tension values, where a narrow strain range permits field-induced superconductivity.

To investigate the origin of the field-induced superconductivity, we performed simultaneous resistivity and XMCD measurements versus field at five fixed strain states between maximum compression and tension (Fig. 5, E and F). Here, the XMCD signal is proportional to the Eu magnetization along the field direction (see Materials and Methods). As the Eu ferromagnetic moments are spontaneously ordered along the *c* axis, the Eu in-plane moment (and XMCD signal) is initially nearly zero under zero field. For all strains, increasing the magnetic field linearly increases the in-plane moment toward saturation at μ_0H_{sat} = 0.25 T, coinciding with the magnetoresistance minimum. From this, we conclude that the Eu moment reorientation toward the in-plane direction is intimately connected to field-induced superconductivity. Despite the large change in the zero-field resistivity with strain, there is no apparent strain-induced change in either the saturation field value or saturation XMCD value. This strain independence is unexpected given that the localized Eu 4f electrons presumably order with assistance from the strain-sensitive Fe 3d electrons via an RKKY interaction (*33*). As strain does not affect the Eu magnetic order, and as strain is far more effective than magnetic field in tuning the nematic order in this material system (*34*), we find that strain and field act as independent tuning parameters of superconductivity.

Dipole coupling and the mechanism of field-induced superconductivity

The antiferromagnetic $EuFe_2As_2$ parent compound has a strong biquadratic interaction between Eu and Fe moments, manifesting as a large magnetostructural coupling (*34*–*36*). The presumed weakening of this coupling with doping causes the Eu moments to become spontaneously polarized along the *c* axis, which would naively be expected to create a strong exchange splitting that destroys the superconductivity. The Jaccarino-Peter effect (*37*) has often been invoked to explain field-induced superconductivity in s-wave superconductors, including in Eu-based Chevrel phases (*9*, *10*) and organic superconductors (*15*, *16*, *38*). Here, the Zeeman splitting induced by an external field compensates the internal exchange-bias splitting, resulting in superconductivity. However, in our experiment, the exchange-bias field is parallel to the external field, so a Jaccarino-Peter compensation is not possible. Instead, two other mechanisms contribute to the exchange splitting induced in the Fe bands: the Hund's rule coupling of Eu f- and d-orbitals, with the latter overlapping with Fe d-orbitals and inducing a polarization parallel to Eu f moments, and the Schrieffer-Wolfe coupling of Eu f-

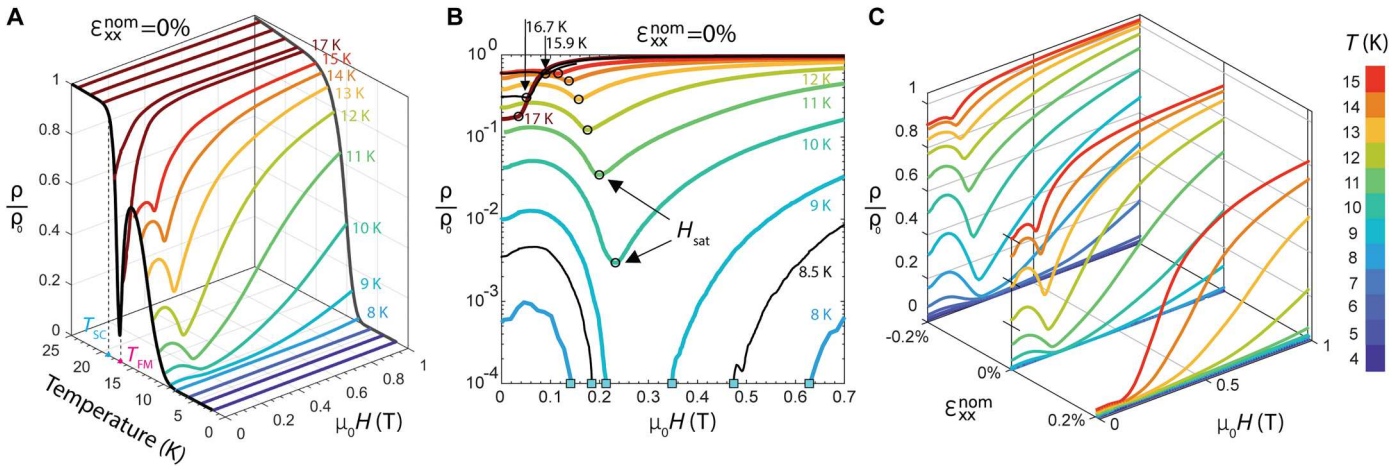

Fig. 3. Strain-tunable field-induced superconductivity. (**A**) Freestanding ($\varepsilon_{xx} = 0$) resistivity versus temperature at fixed in-plane applied field ($\mu_0 H = 0$ T, black; $\mu_0 H = 1$ T, gray) and resistivity versus in-plane field at fixed temperature. Onset of superconducting transition ($T_{SC} = 19$ K) and ferromagnetic order ($T_{FM} = 17.2$ K) indicated. (**B**) Same resistivity versus field data as in (A) plotted against logarithm *y* axis, with additional data at three non-integer temperatures (black). Cyan markers indicate entrance and exit from zero-resistance state for $T = 8$ to 9 K. Minimum of resistivity for $T = 10$ to 16.7 K and inflection point at 17 K marked by black circles, corresponding to the in-plane saturation field H_{sat} needed to align the Eu moments in plane. Entrance and exit from zero-resistance state marked by cyan squares. (**C**) Resistivity versus field at fixed temperatures (4 to 15 K) for one tensile and one compressive strain state and corresponding freestanding values from (A). Field range of zero resistance shown in Fig. 4 (shaded).

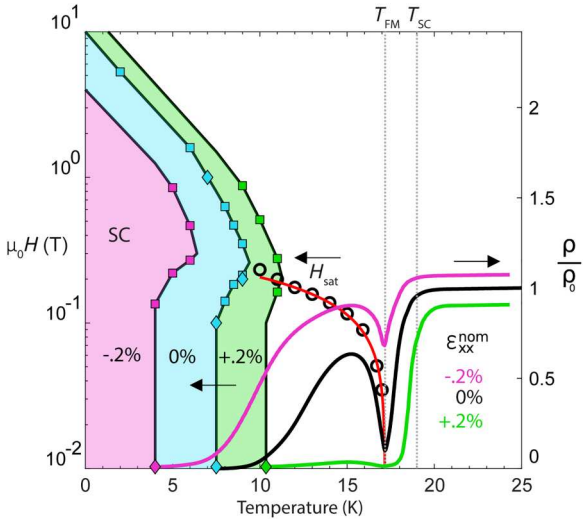

Fig. 4. Strain and field-tunable phase diagram. (**Right**) Resistivity versus temperature for the zero-strain state (same as black curve in Figs. 2 and 3) and for the tensile (green) and compressive (magenta) strain states in Fig. 3C. (**Left**) Phase boundary between $\rho > 0$ and $\rho = 0$ states under zero strain (cyan), tension (green), and compression (magenta), determined by resistivity versus temperature data (diamonds) and resistivity versus magnetic field (squares) from Fig. 3 and fig. S5. Field-induced superconductivity indicated by shaded areas for each strain state. Eu in-plane saturation field H_{sat} taken from minimum of magnetoresistance in Fig. 3B versus temperature (black circles), with mean-field fit line (red).

and Fe d-orbitals, which leads to an antiparallel polarization. To characterize these two effects, we performed DFT calculations using the Wien2K package (*39*, *40*) for Eu moments fully polarized in plane (figs. S8 to S10). We find that both show high sensitivity to the Hubbard U on Eu sites, and as these two interactions have opposite signs, the induced splitting of Fe bands is relatively small and varying in sign and amplitude over the Fermi surface. This "accidental cancelation" gives a reasonable explanation for the coexistence of superconductivity and ferromagnetism. Above T_{FM}, this cancellation is lifted as the Eu moments disorder, which also explains the flipped field preference of superconductivity above and below T_{FM} (Fig. 2 and fig. S5). The weak exchange interaction has previously been suggested by DFT, Mossbauer, and magneto-optic studies in related materials (*23*, *41*–*43*).

An explanation to the field-induced superconductivity mechanism comes by considering both the sizeable dipolar magnetic field exhorted by Eu moments onto the Fe layers and the directional anisotropy of the upper critical field. Using the classical Clausius-Mosotti theory of polarizable media, we determine the dipole field from the stacked infinite planes of fully ordered ferromagnetic Eu moments as $B_{Eu} = m/3v = 0.3$T, where $m = 7\ \mu_B$ is the magnetization of the Eu moments and $v = 90$ Å^3 is the volume per moment. This is not an "effective" magnetic field derived from the exchange splitting, but a real field (with respect to the superconducting condensate) that can be screened by Abrikosov vortices (*3*, *4*, *44*, *45*). At 10 K and an applied field of 0.25 T, the XMCD signal saturates at 80% of the 2K XMCD value (fig. S4), suggesting a total dipole field of 0.24 T, in agreement with this estimate. A resistive state is found under zero field, where a net 0.24 T of Eu field is aligned to the *c* axis. Zero resistance is found under an applied field of 0.25 T in plane, which combines with the reoriented Eu moments to give a total 0.49 T of flux in plane. As in other iron-based superconductors (*46*), $Eu(Fe_{0.88}Co_{0.12})_2As_2$ has a moderate in- versus out-of-plane H_{C2} anisotropy, with $\gamma = H_{C2,in}/H_{C2,out} \cong 2.1$ at $T = 2$ K (fig. S5). As $\gamma > \frac{0.49\ T}{0.25\ T}$, and as we expect γ to increase with temperature toward T_{SC} (*47*), we can explain the narrow field range of the field-induced superconductivity as due primarily to rotating the Eu moments in plane to take advantage of the higher in-plane critical field. Further, this explains why applied strain does not shift the

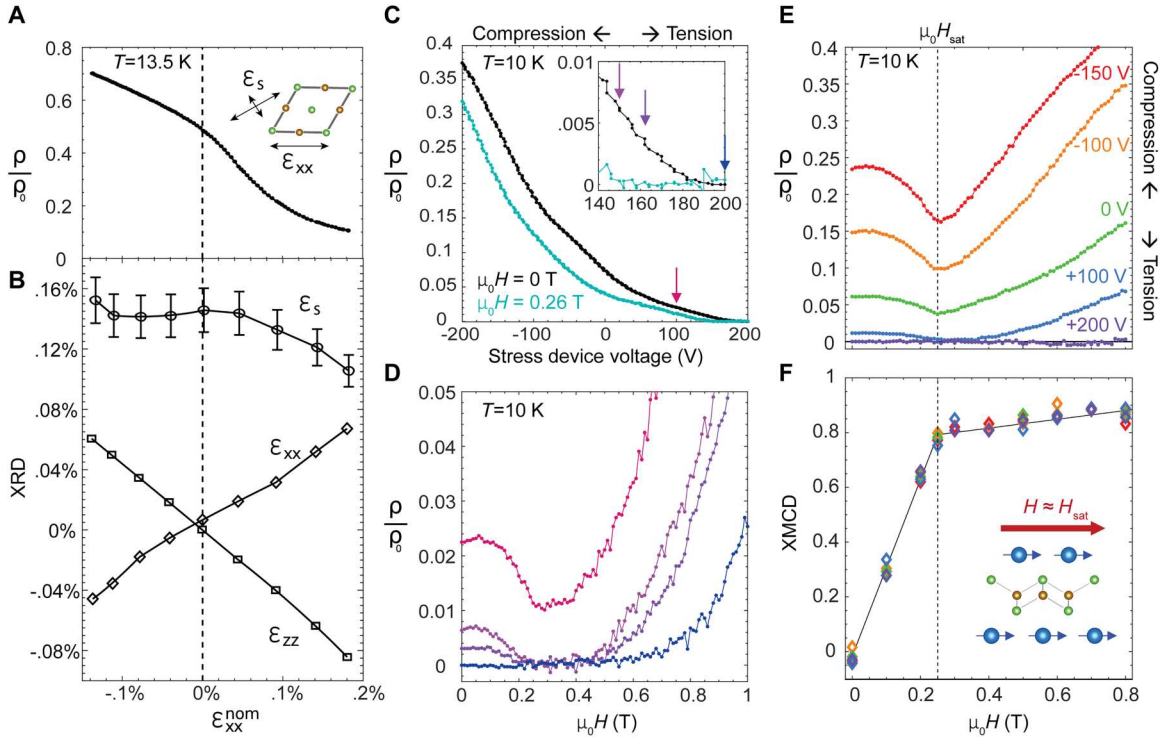

Fig. 5. X-ray characterization of independent strain and field tuning. (**A** and **B**) Fixed temperature (T = 13.5 K) strain sweep (compressive to tensile) with simultaneous (A) resistivity measurements and (B) XRD measurements of the inline strain ε_{xx}, the out-of-plane strain ε_{zz}, and the nematicity-driven spontaneous orthorhombicity ε_S (see Materials and Methods for definitions). (**C**) Resistivity versus strain device voltage at T = 10 K under in-plane applied field of $\mu_0 H$ = 0 T and $\mu_0 H$ = 0.26 T. Inset shows high tension range. The voltage range in (C) corresponds approximately to the range of ε_{xx}^{nom} in (A) and (B), but could not be simultaneously measured due to sample chamber restrictions. (**D**) Resistivity versus applied in-plane field at fixed strain values corresponding to colored arrows in (C) (inset). (**E** and **F**) The simultaneously collected resistivity (E) and XMCD (F) versus applied field at T = 10 K for five fixed strain values (see Materials and Methods for XMCD normalization details). Eu moment saturation coincides with minimum of resistivity at $H = H_{sat}$. Voltages listed in (E) and (F) correspond to slightly greater tension states than corresponding voltages in (C) due to different thermal hysteresis in the piezo actuators between the two measurements. A small negative background magnetoresistance was removed from data in (E) (see Materials and Methods). Error bars in (B) on ε_S represent error propagation of Gaussian fits to the split $[1\ 1\ 8]_T$ reflection peak (see Materials and Methods), while error bars on ε_{xx} and ε_{zz} are smaller than marker size.

field range where superconductivity onsets, as strain does not directly tune the Eu magnetic order.

DISCUSSION

Here, we present field-induced superconductivity between 4 and 10 K, which is enabled with small fields ($\mu_0 H \leq 0.1$ to 0.3 T) and tuned with accessible strain values ($|\varepsilon_{xx}| < 0.2\%$). Our combined XRD, XMCD, and transport measurements show that strain and magnetic field act as independent tuning knobs, with the former affecting the nematic order and Fe antiferromagnetism and the latter affecting the Eu ferromagnetism. These knobs tune the phase diagram analogously to chemical doping, but without introducing additional disorder. The high tunability of this system results from the close competition between the simultaneously coexisting superconducting, nematic, and ferromagnetic phases. In contrast, no field-induced superconductivity has been reported in related Eu-based iron pnictide materials such as $EuRbFe_4As_4$ (*48*) or optimal Ir-doped $EuFe_2As_2$ (*19*), likely due to stronger superconducting order. We anticipate that even higher field-induced superconducting temperatures could be obtained in materials engineered with a perfect balance between higher temperature superconductivity and ferromagnetism.

We further show how the external field-tunable Eu dipole field has a dominant effect on superconductivity when the Eu-Fe exchange splitting is sufficiently weak. This creates a novel mechanism for field-induced superconductivity distinct from the Jaccarino-Peter effect and spin-triplet U-based compounds. This mechanism could likely be present in other systems that exhibit (i) large magnetic moments that are easily field tunable (e.g., L = 0 rare earth elements) and (ii) a superconducting order that is dimensionally highly anisotropic [e.g., a van der Waals (vdW) material (*49*–*51*) or at the interface between different materials (*52*)]. This mechanism could arise quite naturally from a vdW heterostructure, with one superconducting layer and one ferromagnetic layer. We note that the apparent first report of field-reentrant superconductivity in a vdW system occurs with stacked thin flakes of antiferromagnetic $CrCl_3$ and superconducting $NbSe_2$ (*53*), which demonstrates the potential for our proposed mechanism to likewise underlie field-induced superconductivity in 2D materials. Finally, the interaction of ferromagnetism and superconductivity in the presence of very weak exchange splitting has not been widely investigated, yet it may help inform the microscopic understanding of other

phenomena. For instance, a recent investigation of $EuRbFe_4As_4$ encountered a spatially modulated superconducting gap, which is presumably triggered by the Eu ferromagnetism (*54*). The proposed explanation of a Fulde, Ferrel, Larkin, and Ovchinnikov (FFLO) phase appears to have some foundational theoretical challenges, which may be resolved by considering the effects of variable and net-cancelling exchange biases, as well as the role the dipole field may play in modulating the superconducting gap.

Using strain as an additional control switch offers new opportunities to combine superconducting spin valves with the emerging field of "straintronics" (*55*). In Fig. 6, we consider a simple conceptual design for a device that pairs a superconducting spin valve with a piezoelectric substrate. Here, a writing applied magnetic field switches the system into a superconducting state, triggering an increase in tension that maintains the superconductivity after the writing field is removed. Such a device acts as a toggle switch and could be used as a relay, tunable sensor, or memory device. Superconducting spin valves are generally not in situ tunable in their temperature or critical fields; instead, ex situ tuning of the material composition/doping, layer thickness, etc., is required to customize their properties. Thus, the exploration of new routes for in situ strain tuning may lead to new conceptual approaches to superconducting information storage and other technologies.

Another direction for future work is to assess this material's potential for superconducting spintronics applications by studying the degree of spin polarization and spin-triplet pairing of the supercurrent as it passes through the field-tunable magnetic layers (*5*–*7*). The orientation of the Eu moments can be tuned to an arbitrary direction, allowing control of the spin polarization axis of the emitted spin triplet Cooper pairs, while strain can switch the supercurrent on and off. Finally, the small resistivity just above T_0 has previously been associated with mobile flux vortices making up a spontaneous vortex liquid phase, with zero resistivity indicating the freezing of these vortices (*3*, *4*). An intriguing possibility to explain the enhanced strain tunability of T_0 below T_{FM} is that vortices become pinned at nematic domain boundaries (*56*), which can be tuned in number and size with strain. Strain could then be used to switch between a vortex liquid and vortex ice phase at fixed temperature and in the absence (or presence) of field.

MATERIALS AND METHODS

Sample preparation

Single-crystal samples of $Eu(Fe_{0.88}Co_{0.12})_2As_2$ were grown from a tin flux as described elsewhere (*27*). We used a nonstoichiometric mix ratio of $Eu:(Fe_{0.85}Co_{0.15}):As:Sn$ of 1:8.5:2:19. This ratio resulted in samples with higher zero-resistance temperatures (T_0) compared to the stoichiometric 1:2:2:20 ratio (fig. S1) (*27*). However, there was substantial sample to sample variability in T_0, which may result from doping inhomogeneity. Samples from a given batch could be found that did not achieve zero resistance at any temperature, while samples 1 and 2 were among the samples with the highest value of T_0 in their batches. The composition of sample 1 was measured by energy-dispersive x-ray spectroscopy (EDX) to be 12% Co-doping, despite a nominal doping of 15%, with a nearly homogeneous value across the sample surface (fig. S1B). The samples were cleaved from large as-grown single-crystal plate and cut along the tetragonal [1 0 0] direction into bars with dimensions ~2 × 0.60 × 0.06 mm. Four gold wires were attached with silver epoxy to measure the inline resistivity ρ_{xx} using a standard four-point measurement and an SR830 lock-in amplifier with 1-mA fixed current. Sample 1 was measured in a Quantum Design PPMS. Sample 2 was measured in x-ray–compatible cryostats at Argonne National Laboratory.

A piezo-actuator uniaxial stress device (Razorbill Instruments, CS-100) was used to provide in situ stress. The built-in capacitance strain gauge was used to determine the nominal strain ε_{xx}^{nom} as in (*31*). Sample chamber constraints prevented the measurement of ε_{xx}^{nom} for data presented in Fig. 5 (C to F). Below the nematic transition (T_S = 68 K; fig. S3), structural twin domains form along the Fe-Fe bonding direction ($[1\,1\,0]_T$, with lattice constants a_{or} and b_{or}), with orthorhombicity $\varepsilon_S = \frac{a_{or}-b_{or}}{a_{or}+b_{or}}$. Here, we apply stress along the Fe-As bonding direction ($[1\,0\,0]_T$, with lattice constant a_T), resulting in an inline strain $\varepsilon_{xx} = \frac{\Delta a_T}{a_{T,0}}$ and an out-of-plane strain $\varepsilon_{zz} = \frac{\Delta c}{c_0}$.

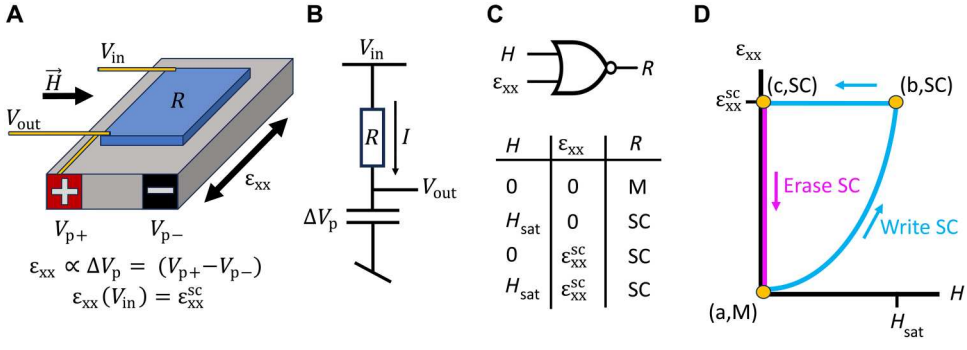

Fig. 6. Conceptual approach for a toggle switch using a strain-switchable superconducting spin valve. (**A**) A field-switchable current divider is created by mechanically and electrically connecting a strain-tunable superconducting spin valve (SSV, blue) to a piezo actuator (gray). (**B**) A current I passes through the SSV from the input (V_{in}) to output (V_{out}) voltage leads, with $V_{out} = V_{in} - IR$. The voltage across the piezo is $\Delta V_p = V_{out}$. (**C**) Device parameters are chosen so that an applied strain $\varepsilon_{xx}(V_{in}) = \varepsilon_{xx}^{SC}$ and/or an applied field $H = H_{sat}$ switches the SSV from a metallic state (M, $R > 0$) to a superconducting state (SC, $R = 0$). (**D**) The circuit initializes at point (a) with the SSV in the M state. Write SC (cyan): A writing magnetic field is applied to switch the SSV from the M state to the SC state. As H increases to H_{sat}, R reduces to zero, which increases the piezo voltage to $\Delta V_p = V_{in}$ and increases the strain to ε_{xx}^{SC} [point (b)]. The additional applied tension maintains the SC state after the writing field is removed [point (c)]. Thus, the device displays memory. Erase SC (magenta): The SSV can be returned to the M state (the written SC state can be erased) by directly discharging the piezo, i.e., by setting $V_{in} = 0$.

The applied stress thus does not detwin the domains, but instead can tune the magnitude of the nematic order parameter through nonlinear couplings between ε_{xx}, ε_{zz}, and ε_S [see (*29*) and figs. S2 and S3].

After mounting sample 1 on the strain device, a field-, strain-, and temperature-dependent background resistivity of order $\rho/\rho_0 \approx 1\%$ was present, masking the true entrance into the zero-resistance state. We estimate the field range of field-induced superconductivity from the field range where the resistivity dips below this background (see figs. S6 and S7 for analysis), from which we estimate that field-induced superconductivity occurs in the bulk of the sample up to $T = 11$ K under maximum tension.

Sample 2 was measured during two separate sample cooldowns, with the first yielding the data in Fig. 5 (E and F) and the second for Fig. 5 (C and D). In the first cooldown, the sample reached zero resistance under zero field. With the application of field, a small negative magnetoresistance background was present due to a cryostat wiring issue. After rewiring the cryostat, true zero resistance under field was measured in sample 2 at $T = 10$ K, reported in Fig. 5 (C and D). The data presented in Fig. 5E were corrected to remove this background through a process discussed in the Supplementary Materials; this correction has a minimal (<0.5%) effect on the resistivity for fields near 0.25 T. The data in Fig. 5 (C and D) are the as-measured data.

XMCD and XRD

XRD measurements were performed at the Advanced Photon Source, beamline 6-ID-B, at Argonne National Laboratory. X-rays of energy 7.6 keV illuminated an area 500 × 500 μm, fully encompassing a cross section of the middle of the crystal where strain transmission is highest. The sample and strain device were mounted on a closed cycle cryostat. Gaussian fits to the tetragonal (1 0 7), (0 0 8), and (1 1 8) reflections were used to determine the lattice constants (a_T), (c), and (a_{or} and b_{or}), corresponding to in plane along the stress axis, out of plane, and in plane at 45° to the stress axis, respectively.

XMCD was measured at the Advanced Photon Source beamline 4-ID-D at Argonne National Laboratory. We probed the Eu L_3 edge using x-rays of 6.97 keV, which measured the spin polarization of the Eu 5d band due primarily to the magnetic moment of the 4f orbital. A superconducting split coil magnet with a large bore was used to apply magnetic field. The sample temperature was controlled using liquid He. XMCD was collected in fluorescence geometry by monitoring the Eu L_α line using a four-element Vortex detector integrated with the Xspress module to enable a larger dynamical range. Circularly polarized x-rays were generated using a 180-μm-thick diamond (111) phase plate. Data were corrected for self-absorption. The XMCD spot size illuminates the whole sample width across the y direction and is roughly 100 μm wide along the x direction (between the transport wires) and probes a depth of about 5 μm. The beam is centered on the middle of the crystal where strain is most transmitted and homogeneous. The incident beam was aligned with the applied magnetic field at an angle of ~10° above parallel to the sample surface (grazing incidence) due to sample chamber constraints. All XMCD data are normalized to the zero-strain, $\mu_0 H > 0.3$ T saturated value at $T = 2$ K (fig. S4).

DFT calculations

The full-potential linearized augmented plane-wave Wien2K package (*39*) has been used for the DFT calculations. We use the Perdew, Burke, and Ernzerhof (*40*) version of the generalized gradient approximation (GGA) to the exchange-correlation functional within DFT. The sphere radii for Eu, Fe, and As are taken as 2.50, 2.29, and 2.18 bohr, respectively. The basis set cutoff parameter RmtKmax = 8.0 was used. The number of k points was set to 4500. The crystal structure and magnetic moments on Eu and Fe are illustrated in fig. S8. We set $U = 9$ eV on the Eu atom and did collinear spin-polarized self-consistent calculations in the primitive (not conventional) cell. WIEN2k has a parameter (κ) that tweaks the strength of Hund's rule coupling. The Hund's rule coupling is set to normal full strength when κ = 1 and completely switches off when κ = 0. We used this parameter to delineate the two effects mentioned above: The Schrieffer-Wolfe interaction does not depend on the Hund's rule coupling strength, while the Eu(f)–Eu(d) interaction can be switched off using κ. In fig. S9, we show the band structure for these two values of κ around the Fermi level. The largest splitting near the Fermi level when κ = 1 is about 25 meV along ΓZ-.

Supplementary Materials

This PDF file includes:

Supplementary Text
Figs. S1 to S14
References

REFERENCES AND NOTES

1. D. N. Basov, R. D. Averitt, D. Hsieh, Towards properties on demand in quantum materials. *Nat. Mater.* **16**, 1077–1088 (2017).
2. S. Nandi, W. T. Jin, Y. Xiao, Y. Su, S. Price, D. K. Shukla, J. Strempfer, H. S. Jeevan, P. Gegenwart, T. Brückel, Coexistence of superconductivity and ferromagnetism in P-doped $EuFe_2As_2$. *Phys. Rev. B* **89**, 014512 (2014).
3. W.-H. Jiao, Q. Tao, Z. Ren, Y. Liu, G.-H. Cao, Evidence of spontaneous vortex ground state in an iron-based ferromagnetic superconductor. *npj Quantum Mater.* **2**, 50 (2017).
4. V. S. Stolyarov, I. S. Veshchunov, S. Y. Grebenchuk, D. S. Baranov, I. A. Golovchanskiy, A. G. Shishkin, N. Zhou, Z. Shi, X. Xu, S. Pyon, Y. Sun, W. Jiao, G.-H. Cao, L. Y. Vinnikov, A. A. Golubov, T. Tamegai, A. I. Buzdin, D. Roditchev, Domain Meissner state and spontaneous vortex-antivortex generation in the ferromagnetic superconductor $EuFe_2(As_{0.79}P_{0.21})_2$. *Sci. Adv.* **4**, eaat1061 (2018).
5. J. Linder, J. W. A. Robinson, Superconducting spintronics. *Nat. Phys.* **11**, 307–315 (2015).
6. G. D. Simoni, E. Strambini, J. S. Moodera, F. S. Bergeret, F. Giazotto, Toward the absolute spin-valve effect in superconducting tunnel junctions. *Nano Lett.* **18**, 6369–6374 (2018).
7. M. G. Flokstra, N. Satchell, J. Kim, G. Burnell, P. J. Curran, S. J. Bending, J. F. K. Cooper, C. J. Kinane, S. Langridge, A. Isidori, N. Pugach, M. Eschrig, H. Luetkens, A. Suter, T. Prokscha, S. L. Lee, Remotely induced magnetism in a normal metal using a superconducting spin-valve. *Nat. Phys.* **12**, 57–61 (2016).
8. B. Li, N. Roschewsky, B. A. Assaf, M. Eich, M. Epstein-Martin, D. Heiman, M. Münzenberg, J. S. Moodera, Superconducting spin switch with infinite magnetoresistance induced by an internal exchange field. *Phys. Rev. Lett.* **110**, 097001 (2013).
9. H. W. Meul, C. Rossel, M. Decroux, Ø. Fischer, G. Remenyi, A. Briggs, Observation of magnetic-field-induced superconductivity. *Phys. Rev. Lett.* **53**, 497–500 (1984).
10. J. Cors, R. Baíllif, M. G. Karkut, M. Decroux, Ø. Fischer, U. Welp, G. Bruls, Observation of magnetic-field-induced superconductivity in Se-doped EuMo6S8 under pressure. *Europhys. Lett.* **3**, 635–641 (1987).
11. F. Lévy, I. Sheikin, B. Grenier, A. D. Huxley, Magnetic field-induced superconductivity in the ferromagnet URhGe. *Science* **309**, 1343–1346 (2005).
12. P. T. Yang, Z. Y. Liu, K. Y. Chen, X. L. Liu, X. Zhang, Z. H. Yu, H. Zhang, J. P. Sun, Y. Uwatoko, X. L. Dong, K. Jiang, J. P. Hu, Y. F. Guo, B. S. Wang, J.-G. Cheng, Pressured-induced superconducting phase with large upper critical field and concomitant enhancement of antiferromagnetic transition in $EuTe_2$. *Nat. Commun.* **13**, 2975 (2022).
13. G. Knebel, W. Knafo, A. Pourret, Q. Niu, M. Vališka, D. Braithwaite, G. Lapertot, M. Nardone, A. Zitouni, S. Mishra, I. Sheikin, G. Seyfarth, J.-P. Brison, D. Aoki, J. Flouquet, Field-reentrant

superconductivity close to a metamagnetic transition in the heavy-fermion superconductor UTe_2. *J. Physical Soc. Japan* **88**, 063707 (2019).
14. S. Ran, S. R. Saha, I. L. Liu, D. Graf, J. Paglione, N. P. Butch, Expansion of the high field-boosted superconductivity in UTe_2 under pressure. *npj Quantum Mater.* **6**, 75 (2021).
15. T. Konoike, S. Uji, T. Terashima, M. Nishimura, S. Yasuzuka, K. Enomoto, H. Fujiwara, B. Zhang, H. Kobayashi, Magnetic-field-induced superconductivity in the antiferromagnetic organic superconductor κ−$(BETS)_2FeBr_4$. *Phys. Rev. B* **70**, 094514 (2004).
16. K. Hiraki, H. Mayaffre, M. Horvatić, C. Berthier, S. Uji, T. Yamaguchi, H. Tanaka, A. Kobayashi, H. Kobayashi, T. Takahashi, ^{77}Se NMR evidence for the jaccarino–Peter mechanism in the field induced superconductor, λ-$(BETS)_2FeCl_4$. *J. Physical Soc. Japan* **76**, 124708 (2007).
17. S. Jiang, H. Xing, G. Xuan, Z. Ren, C. Wang, Z. Xu, G. Cao, Superconductivity and local-moment magnetism in $Eu(Fe_{0.89}Co_{0.11})_2As_2$. *Phys. Rev. B* **80**, 184514 (2009).
18. U. B. Paramanik, P. L. Paulose, S. Ramakrishnan, A. K. Nigam, C. Geibel, Z. Hossain, Magnetic and superconducting properties of Ir-doped $EuFe_2As_2$. *Supercond. Sci. Technol.* **27**, 075012 (2014).
19. W.-H. Jiao, H.-F. Zhai, J.-K. Bao, Y.-K. Luo, Q. Tao, C.-M. Feng, Z.-A. Xu, G.-H. Cao, Anomalous critical fields and the absence of Meissner state in $Eu(Fe_{0.88}Ir_{0.12})_2As_2$ crystals. *New J. Phys.* **15**, 113002 (2013).
20. H. S. Jeevan, D. Kasinathan, H. Rosner, P. Gegenwart, Interplay of antiferromagnetism, ferromagnetism, and superconductivity in $EuFe_2(As_{1-x}P_x)_2$ single crystals. *Phys. Rev. B.* **83**, 054511 (2011).
21. S. Zapf, M. Dressel, Europium-based iron pnictides: A unique laboratory for magnetism, superconductivity and structural effects. *Rep. Prog. Phys.* **80**, 016501 (2017).
22. A. Baumgartner, D. Neubauer, S. Zapf, A. V. Pronin, W. H. Jiao, G. H. Cao, M. Dressel, Re-entrant phases in electron-doped $EuFe_2As_2$: Spin glass and superconductivity. *Phys. Rev. B* **95**, 174522 (2017).
23. I. Nowik, I. Felner, Z. Ren, G. H. Cao, Z. A. Xu, Coexistence of ferromagnetism and superconductivity: Magnetization and Mössbauer studies of $EuFe_2(As_{1-x}P_x)_2$. *J. Phys. Condens. Matter* **23**, 065701 (2011).
24. W.-H. Jiao, J.-K. Bao, Q. Tao, H. Jiang, C.-M. Feng, Z.-A. Xu, G.-H. Cao, Evolution of superconductivity and ferromagnetism in $Eu(Fe_{1-x}Ru_x)_2As_2$. *J. Phys. Conf. Ser.* **400**, 022038 (2012).
25. W. T. Jin, Y. Xiao, Z. Bukowski, Y. Su, S. Nandi, A. P. Sazonov, M. Meven, O. Zaharko, S. Demirdis, K. Nemkovski, K. Schmalzl, L. M. Tran, Z. Guguchia, E. Feng, Z. Fu, T. Brückel, Phase diagram of Eu magnetic ordering in Sn-flux-grown Eu(Fe1−xCox)$_2As_2$ single crystals. *Phys. Rev. B* **94**, 184513 (2016).
26. W. T. Jin, W. Li, Y. Su, S. Nandi, Y. Xiao, W. H. Jiao, M. Meven, A. P. Sazonov, E. Feng, Y. Chen, C. S. Ting, G. H. Cao, T. Brückel, Magnetic ground state of superconducting $Eu(Fe_{0.88}Ir_{0.12})_2As_2$: A combined neutron diffraction and first-principles calculation study. *Phys. Rev. B* **91**, 064506 (2015).
27. V. H. Tran, T. A. Zaleski, Z. Bukowski, L. M. Tran, A. J. Zaleski, Tuning superconductivity in $Eu(Fe_{0.81}Co_{0.19})_2As_2$ with magnetic fields. *Phys. Rev. B* **85**, 052502 (2012).
28. A. Löhle, A. Baumgartner, S. Zapf, M. Dressel, W. H. Jiao, G. H. Cao, Effects of pressure and magnetic field on the reentrant superconductor $Eu(Fe_{0.93}Rh_{0.07})_2As_2$. *Phys. Rev. B.* **95**, 195146 (2017).
29. M. S. Ikeda, T. Worasaran, J. C. Palmstrom, J. A. W. Straquadine, P. Walmsley, I. R. Fisher, Symmetric and antisymmetric strain as continuous tuning parameters for electronic nematic order. *Phys. Rev. B* **98**, 245133 (2018).
30. P. Malinowski, Q. Jiang, J. J. Sanchez, J. Mutch, Z. Liu, P. Went, J. Liu, P. J. Ryan, J.-W. Kim, J.-H. Chu, Suppression of superconductivity by anisotropic strain near a nematic quantum critical point. *Nat. Phys.* **16**, 1189–1193 (2020).
31. J. J. Sanchez, P. Malinowski, J. Mutch, J. Liu, J.-W. Kim, P. J. Ryan, J.-H. Chu, The transport–Structural correspondence across the nematic phase transition probed by elasto X-ray diffraction. *Nat. Mater.* **20**, 1519–1524 (2021).
32. X. Chen, S. Maiti, R. M. Fernandes, P. J. Hirschfeld, Nematicity and superconductivity: Competition versus cooperation. *Phys. Rev. B* **102**, 184512 (2020).
33. A. Akbari, P. Thalmeier, I. Eremin, Evolution of the multiband Ruderman–Kittel–Kasuya–Yosida interaction: Application to iron pnictides and chalcogenides. *New J. Phys.* **15**, 033034 (2013).
34. J. J. Sanchez, G. Fabbris, Y. Choi, Y. Shi, P. Malinowski, S. Pandey, J. Liu, I. I. Mazin, J.-W. Kim, P. Ryan, J.-H. Chu, Strongly anisotropic antiferromagnetic coupling in $EuFe_2As_2$ revealed by stress detwinning. *Phys. Rev. B* **104**, 104413 (2021).
35. S. Zapf, C. Stingl, K. W. Post, J. Maiwald, N. Bach, I. Pietsch, D. Neubauer, A. Löhle, C. Clauss, S. Jiang, H. S. Jeevan, D. N. Basov, P. Gegenwart, M. Dressel, Persistent detwinning of iron-pnictide $EuFe_2As_2$ crystals by small external magnetic fields. *Phys. Rev. Lett.* **113**, 227001 (2014).
36. J. Maiwald, I. I. Mazin, P. Gegenwart, Microscopic theory of magnetic detwinning in iron-based superconductors with large-spin rare earths. *Phys. Rev. X* **8**, 011011 (2018).
37. V. Jaccarino, M. Peter, Ultra-high-field superconductivity. *Phys. Rev. Lett.* **9**, 290–292 (1962).
38. L. Balicas, J. S. Brooks, K. Storr, S. Uji, M. Tokumoto, H. Tanaka, H. Kobayashi, A. Kobayashi, V. Barzykin, L. P. Gor'kov, Superconductivity in an organic insulator at very high magnetic fields. *Phys. Rev. Lett.* **87**, 067002 (2001).
39. P. Blaha, K. Schwarz, F. Tran, R. Laskowski, G. K. H. Madsen, L. D. Marks, WIEN2k: An APW+lo program for calculating the properties of solids. *J. Chem. Phys.* **152**, 074101 (2020).
40. J. P. Perdew, K. Burke, M. Ernzerhof, Generalized gradient approximation made simple. *Phys. Rev. Lett.* **77**, 3865–3868 (1996).
41. I. Nowik, I. Felner, Z. Ren, G. H. Cao, Z. A. Xu, ^{57}Fe and ^{151}Eu Mössbauer spectroscopy and magnetization studies of $Eu(Fe_{0.89}Co_{0.11})_2As_2$ and $Eu(Fe_{0.9}Ni_{0.1})_2As_2$. *New J. Phys.* **13**, 023033 (2011).
42. H. S. Jeevan, Z. Hossain, D. Kasinathan, H. Rosner, C. Geibel, P. Gegenwart, Electrical resistivity and specific heat of single-crystalline $EuFe_2As_2$: A magnetic homologue of $SrFe_2As_2$. *Phys. Rev. B* **78**, 052502 (2008).
43. A. Pogrebna, T. Mertelj, N. Vujičić, G. Cao, Z. A. Xu, D. Mihailovic, Coexistence of ferromagnetism and superconductivity in iron based pnictides: A time resolved magnetooptical study. *Sci. Rep.* **5**, 7754 (2015).
44. V. L. Ginzburg, Ferromagnetic superconductors. *Soviet Physics–JETP* **4**, 153 (1956).
45. Z. Devizorova, S. Mironov, A. Buzdin, Theory of magnetic domain phases in ferromagnetic superconductors. *Phys. Rev. Lett.* **122**, 117002 (2019).
46. M. Kano, Y. Kohama, D. Graf, F. Balakirev, A. S. Sefat, M. A. Mcguire, B. C. Sales, D. Mandrus, S. W. Tozer, Anisotropy of the upper critical field in a co-doped $BaFe_2As_2$ single crystal. *J. Physical Soc. Japan* **78**, 084719 (2009).
47. N. Ni, M. E. Tillman, J.-Q. Yan, A. Kracher, S. T. Hannahs, S. L. Bud'ko, P. C. Canfield, Effects of Co substitution on thermodynamic and transport properties and anisotropic H_{c2} in $Ba(Fe_{1-x}Co_x)_2As_2$ single crystals. *Phys. Rev. B* **78**, 214515 (2008).
48. M. Hemmida, N. Winterhalter-Stocker, D. Ehlers, H.-A. K. von Nidda, M. Yao, J. Bannies, E. D. L. Rienks, R. Kurleto, C. Felser, B. Büchner, J. Fink, S. Gorol, T. Förster, S. Arsenijevic, V. Fritsch, P. Gegenwart, Topological magnetic order and superconductivity in $EuRbFe_4As_4$. *Phys. Rev. B* **103**, 195112 (2021).
49. X. Xi, Z. Wang, W. Zhao, J.-H. Park, K. T. Law, H. Berger, L. Forró, J. Shan, K. F. Mak, Ising pairing in superconducting $NbSe_2$ atomic layers. *Nat. Phys.* **12**, 139–143 (2016).
50. J. M. Lu, O. Zheliuk, I. Leermakers, N. F. Q. Yuan, U. Zeitler, K. T. Law, J. T. Ye, Evidence for two-dimensional Ising superconductivity in gated MoS_2. *Science* **350**, 1353–1357 (2015).
51. W. Fang, K. D. Belashchenko, M. Haim, M. Khodas, I. I. Mazin, Interplay of magnetic field and magnetic impurities in Ising superconductors. arXiv: 2306.01700 [cond-mat.supr-con] (2 June 2023).
52. E. G. Arnault, A. H. Al-Tawhid, S. Salmani-Rezaie, D. A. Muller, D. P. Kumah, M. S. Bahramy, G. Finkelstein, K. Ahadi, Anisotropic superconductivity at $KTaO_3$(111) interfaces. *Sci. Adv.* **9**, eadf1414 (2023).
53. D. Jiang, T. Yuan, Y. Wu, X. Wei, G. Mu, Z. An, W. Li, Strong In-plane magnetic field-induced reemergent superconductivity in the van der waals heterointerface of $NbSe_2$ and $CrCl_3$. *ACS Appl. Mater. Interfaces* **12**, 49252–49257 (2020).
54. H. Zhao, R. Blackwell, M. Thinel, T. Handa, S. Ishida, X. Zhu, A. Iyo, H. Eisaki, A. N. Pasupathy, K. Fujita, Smectic pair-density-wave order in $EuRbFe_4As_4$. *Nature* **618**, 940–945 (2023).
55. A. A. Bukharaev, A. K. Zvezdin, A. P. Pyatakov, Y. K. Fetisov, Straintronics: A new trend in micro- and nanoelectronics and materials science. *Phys. Usp.* **61**, 1175–1212 (2018).
56. R. Prozorov, M. A. Tanatar, N. Ni, A. Kreyssig, S. Nandi, S. L. Bud'ko, A. I. Goldman, P. C. Canfield, Intrinsic pinning on structural domains in underdoped single crystals of Ba $(Fe_{1-x}Cox)_2As_2$. *Phys. Rev. B* **80**, 174517 (2009).
57. G. Wang, W. R. Meier, W. E. Straszheim, J. Slagle, S. L. Bud'ko, P. C. Canfield, Lack of superconductivity in the phase diagram of single-crystalline $Eu(Fe_{1-x}Co_x)_2As_2$ grown by transition metal arsenide flux. *Phys. Rev. Mater.* **2**, 104801 (2018).

Acknowledgments: We thank R. Comin, C. Occhialini, L. Powalla, X. Wang, S. Y. F. Zhao, A. Chen, C. John, J. Analytis, C. Ross, and J. Moodera for useful conversation. **Funding:** This study was supported by the Air Force Office of Scientific Research under grant FA9550-21-1-0068 and the David and Lucile Packard Foundation (J.J.S., J.M.D., E.R., Y.S., P.M., and J.-H.C.); U.S. Department of Energy (DOE), Office of Science, and Office of Basic Energy Sciences, Contract No. DE-AC02-06CH11357 (G.F., Y.C., J.-W.K., and P.J.R.); U.S. Department of Energy (DOE), grant no. DE-SC0021089 (I.I.M.); National Natural Science Foundation of China, grant no.11904319. (Y.H.); and National Science Foundation MPS-Ascend Postdoctoral Research Fellowship, Award No. 2138167 (J.J.S.). Any opinions, findings, and conclusions or recommendations expressed in this material are those of the author(s) and do not necessarily reflect the views of the National Science Foundation. **Author contributions:** J.J.S. conceived the project and wrote the paper, with input from all authors. J.J.S. and Y.S. grew the samples. J.J.S., J.M.D., E.R., Y.S., and P.M. performed all nonsynchrotron transport measurements. J.J.S., G.F., Y.C., J.-W.K., and P.J.R. performed all synchrotron measurements. The field-induced superconductivity mechanism

proposed in this paper was conceived by J.J.S. and further developed by I.I.M., while Y.H. and I.I. M. performed DFT calculations. J.-H.C. and P.J.R. supervised the project. **Competing interests:** The authors declare that they have no competing interests. **Data and materials availability:** The figure data for this study have been deposited in the Dryad Data Repository with identifier doi: 10.5061/dryad.2280gb5zx. All other data needed to evaluate the conclusions in the paper are present in the paper and/or the Supplementary Materials.

Submitted 30 June 2023
Accepted 26 October 2023
Published 24 November 2023
10.1126/sciadv.adj5200

Science Advances

Strain-switchable field-induced superconductivity

Joshua J. Sanchez, Gilberto Fabbris, Yongseong Choi, Jonathan M. DeStefano, Elliott Rosenberg, Yue Shi, Paul Malinowski, Yina Huang, Igor I. Mazin, Jong-Woo Kim, Jiun-Haw Chu, and Philip J. Ryan

Sci. Adv. **9** (47), eadj5200. DOI: 10.1126/sciadv.adj5200

Science Advances (ISSN 2375-2548) is published by the American Association for the Advancement of Science. 1200 New York Avenue NW, Washington, DC 20005. The title *Science Advances* is a registered trademark of AAAS.

Science Advances
AAAS

Supplementary Materials for

Strain-switchable field-induced superconductivity

Joshua J. Sanchez *et al.*

Corresponding author: Joshua J. Sanchez, sanchezx@mit.edu; Jiun-Haw Chu, jhchu@uw.edu; Philip J. Ryan, pryan@anl.gov

Sci. Adv. **9**, eadj5200 (2023)
DOI: 10.1126/sciadv.adj5200

This PDF file includes:

Supplementary Text

I. Crystal Growth

Single crystal samples of $\mathrm{Eu(Fe_{0.85}Co_{0.15})_2As_2}$ were grown from a tin flux as described elsewhere (*27*). We used a nonstoichiometric mix ratio of $\mathrm{Eu{:}\ (Fe_{0.85}Co_{0.15}){:}\ As{:}\ Sn}$ of 1:8.5:2:19. This ratio resulted in samples with higher zero-resistance temperatures ($\mathrm{T_0}$) compared to the stoichiometric 1:2:2:20 ratio (Fig.S1a). However, energy dispersive x-ray spectroscopy (EDX) measurements suggest the Co-doping to be 12% instead of the nominal 15% (Fig.S1b). The superconducting properties of doped $EuFe_2As_2$ depend sensitively on growth methods. For instance, no superconductivity is found for Co-doped samples grown by FeAs flux (*57*). Further investigation of the non-stoichiometric growth conditions is warranted.

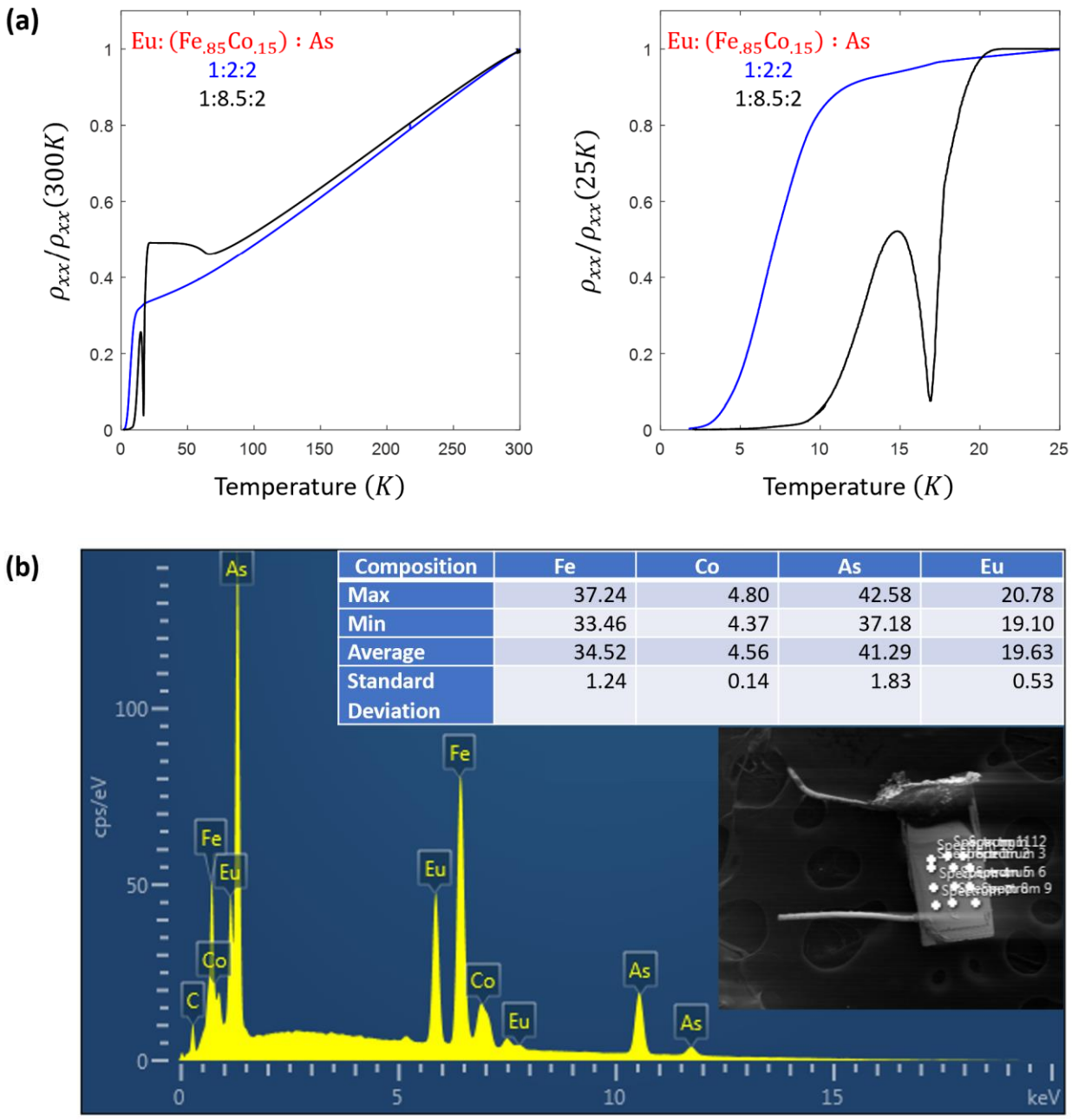

Figure S1. Transport and Composition Characterization.

(a) Comparison of resistivity vs temperature for samples grown with an elemental composition that was stoichiometric (blue) and nonstoichiometric (black; sample 2 from main text). **(b)** Sample 1. EDX spectra at 12 points on surface. EDX was performed after removing sample 1 from the strain device after all transport measurements were completed (note the still-attached gold wire). No trace of the Sn flux used in the crystal growth is evident. The nominal composition was Fe=0.85, Co=0.15, while the EDX measured composition was Fe=0.88, Co=0.12.

II. XRD under strain

XRD measurements were performed on sample 2 at the Advanced Photon Source, beamline 6-ID-B, at Argonne National Laboratory. X-rays of energy 7.6 keV illuminated an area 500x500 um, fully encompassing a cross section of the middle of the crystal where strain transmission is highest. The sample and strain device were mounted on a closed cycle cryostat. Gaussian fits to the tetragonal $(1\ 0\ 7)$, $(0\ 0\ 8)$ and $(1\ 1\ 8)$ reflections were used to determine the lattice constants (a_T), (c), and (a_{Or} & b_{Or}, due to the split peak in the twinned state), corresponding to in-plane along the stress axis, out of plane, and in-plane at 45 degrees to the stress axis, respectively.

Figure S2 shows the uniaxial strains $\frac{\Delta a_T}{a_T}$ and $\frac{\Delta c_T}{c_T}$ and the nematic-driven spontaneous orthorhombicity $\varepsilon_S = \frac{a_{Or}-b_{Or}}{a_{Or}+b_{Or}}$ as a function of strain at T=13.5 K. We observe that $\varepsilon_{xx} = \frac{\Delta a_T}{a_{T,0}}$ is roughly linear to ε_{xx}^{nom} determined from the capacitive strain gauge of the stress device. We find a nearly constant strain transmission of $\frac{d\varepsilon_{xx}}{d\varepsilon_{xx}^{nom}}$ =34% across the range of the strains applied. The out of plane uniaxial strain $\varepsilon_{zz} = \frac{\Delta c}{c_0}$ is surprisingly large compared to ε_{xx} with the Poisson ratio $\nu_{xz} = -\frac{d\varepsilon_{zz}}{d\varepsilon_{xx}}|_{\varepsilon_{xx}=0}$ approaching 1.3. A Poisson's ratio greater than unity is unexpected in an isotropic, linear elastic material, and so this large change in planar spacing may result from a substantial magnetostructural response due to the ferromagnetic Eu layers, as well as tuning of the nematic order.

Most importantly, ε_S is found to be suppressed by roughly 30% at maximum tension, while being relatively unaffected (or even slightly enhanced) by compression. Given the competition between nematic order and superconductivity, it is clear that the sharp reduction in the resistivity with tension can be attributed (at least in part) by a strain-suppression of the nematic order (see also Fig.S6a). This result is fully in agreement with previous work in Co-doped $BaFe_2As_2$, where tension (compression) applied along the tetragonal [1 0 0] direction resulted in a suppression (enhancement) of the nematic transition temperature (*29*). We observe a similar effect via warming the sample through the nematic transition under either tension or compression (Figure S3). Phenomenologically, the tuning of nematicity with stress applied along the tetragonal [1 0 0] direction results both from the introduction of an orthogonal antisymmetric strain $\left(\varepsilon_{B_{1g}} = \frac{a_T-b_T}{a_T+b_T}\right)$ which acts to suppress nematicity and ε_S, and to a surprisingly large sensitivity to ε_{zz} which tunes the unit cell volume despite not breaking any symmetries (see ref. (*29*)).

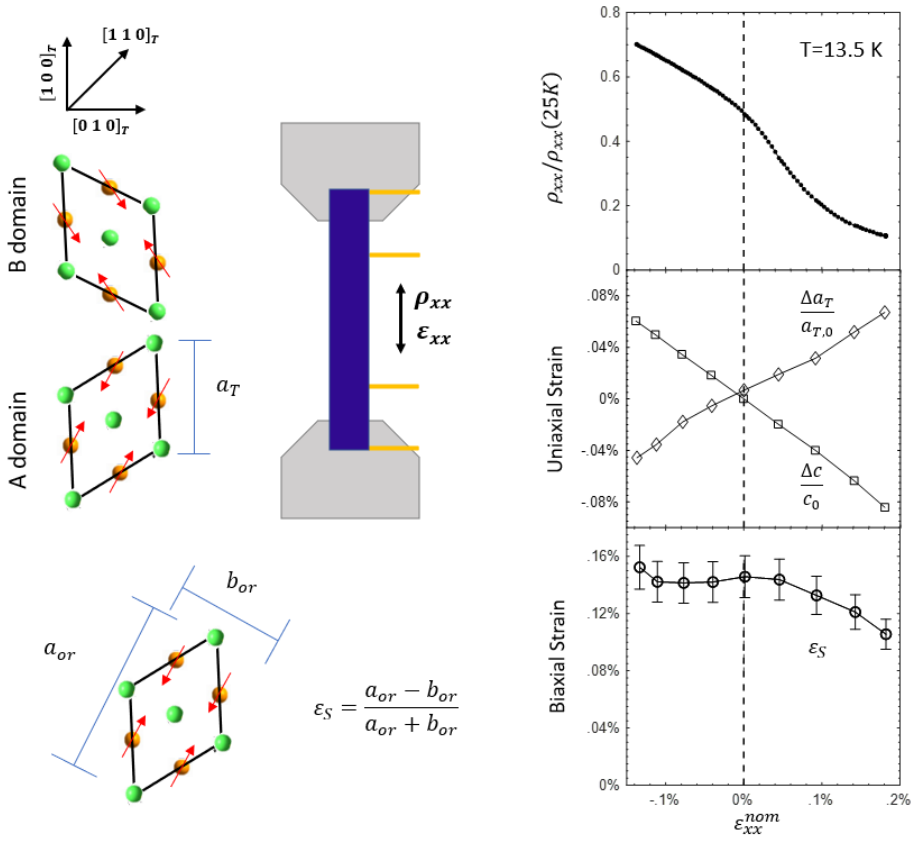

Figure S2. X-ray Diffraction Under Strain.

Sample 2. Fixed temperature (T=13.5K) strain sweep (compressive to tensile) with simultaneous resistivity measurements and XRD measurements of the a_T and c lattice constants (presented normalized by their zero-strain values) and the a_{Or} and b_{Or} lattice constants (presented as the antisymmetric strain ε_S). Error bars on ε_S represent the error propagation of the Gaussian fits to a_{Or} and b_{Or}.

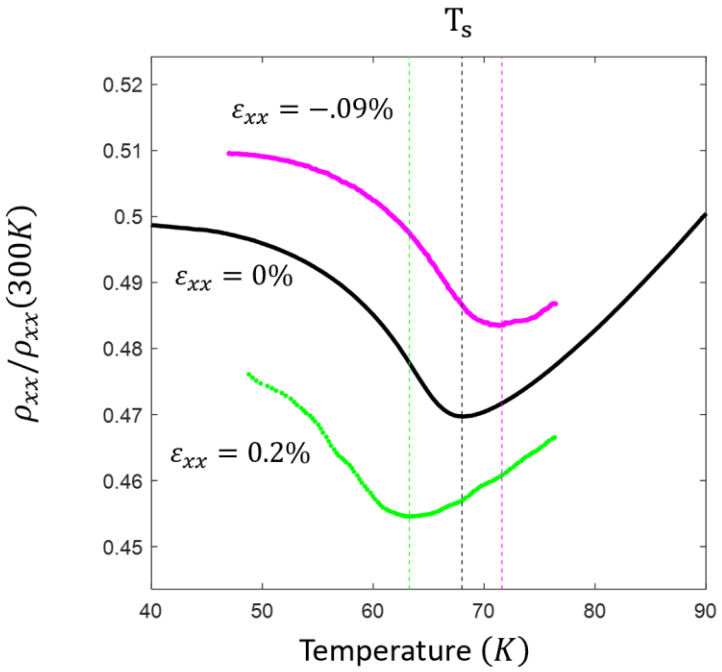

Figure S3. Strain-tuning the nematic transition.

Sample 2. Resistivity vs temperature under zero strain (black, freestanding data from Fig.S1), tension (green) and compression (magenta). Note: the fixed-strain data has been corrected for a ~3 K thermal lag. As such, we do not attempt to make a quantitative assessment of the strain-tuning of the transition temperature, and instead only share this data to show the basic phenomenology of an enhanced (suppressed) nematic transition temperature with compression (tension) in qualitative agreement with past work in Co-doped $BaFe_2As_2$ (*29*).

III. XMCD of 2K result

On sample 2, the first XMCD data were taken after the initial cooldown at zero applied strain at T=2 K and 10 K through a field range of μ_0H=+-1 T. All XMCD data in this work are normalized to this μ_0H>0.3 T, T= 2 K fully saturated XMCD value, which corresponds to the $M \sim 7\ \mu_B$ (μ_0H~0.3 T) fully ordered Eu magnetic moment. The initial XMCD saturation value at T=10K, μ_0H=0.25T is approximately 80% of the 2K saturation value. See Main Text for details of the XMCD measurement.

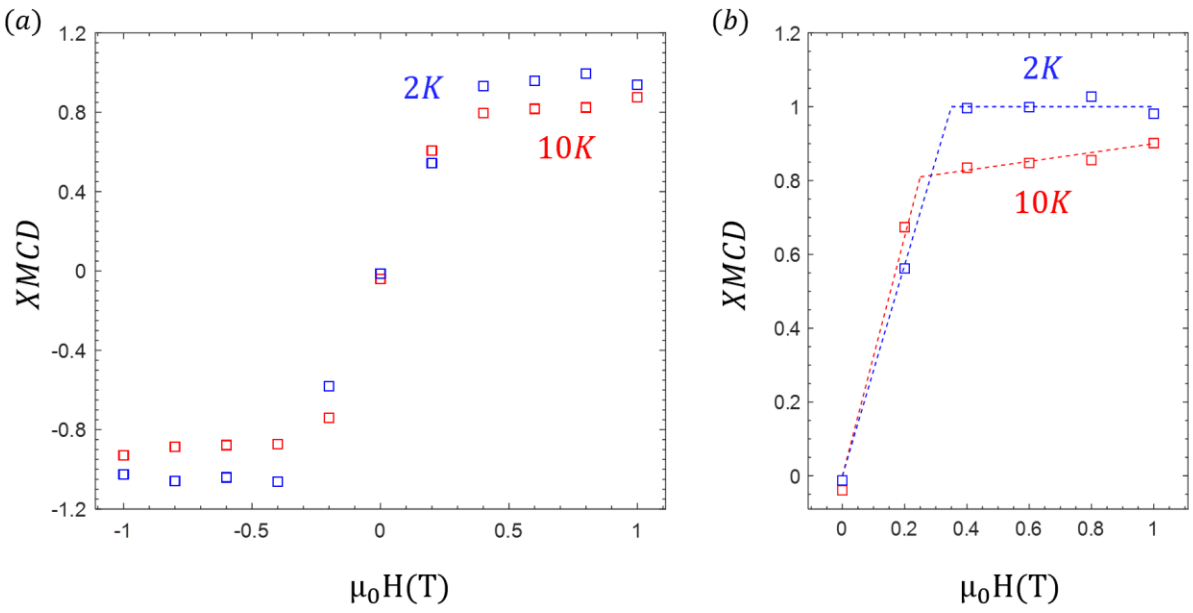

Figure S4. XMCD at 2K and 10K.

Sample 2. XMCD vs field at 2K and 10K. Data in (a) collected from a single field sweep from +1T to -1T. Data in (b) are the normalized difference of the positive and negative field values in (a).

IV. Freestanding magnetoresistance Sample 1

In the freestanding state prior to mounting on the strain cell, sample 1 was cooled through the superconducting and ferromagnetic transitions under zero field (Fig.S5a,b, black), and with an applied field of μ_0H=0.1 T, 0.2 T and 1.0 T either in-plane (Fig.S5a) or out of plane (Fig.S5b). An out of plane field is found to only increase the resistivity, while only lowering the value of T_0. In sharp contrast, an in-plane field is far more detrimental to superconductivity between T_{sc} and T_{FM}, but zero resistance is reached at an enhanced value of T_0=9.0 K for μ_0H=0.2 T, demonstrating field-induced superconductivity.

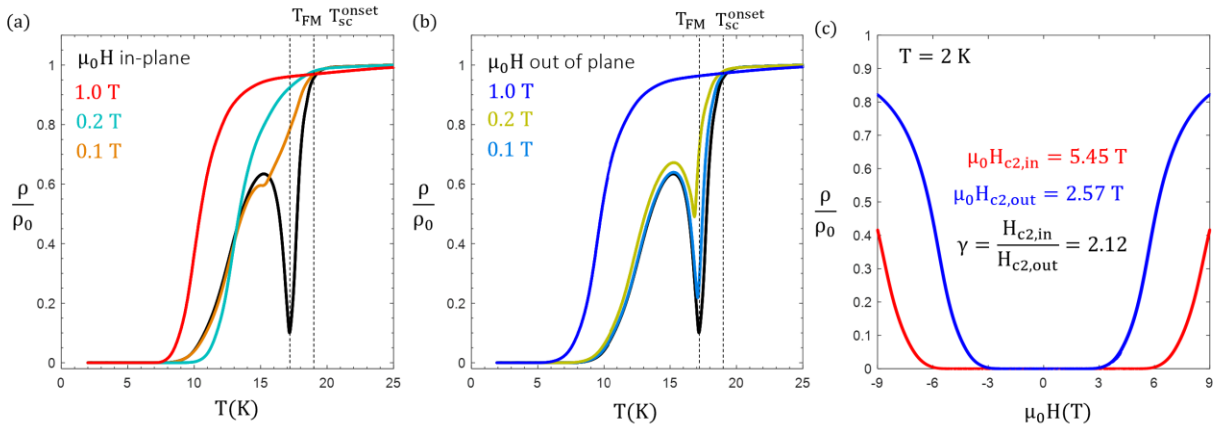

Figure S5. Resistivity for in and out of plane fields.

(a,b) Sample 1. Resistivity vs temperature for zero applied field (black) and $\mu_0 H$ = 0.1T, 0.2T, and 1T applied in-plane **(a)** and out of plane **(b)**. For $\mu_0 H$ = 0.2T, applied in-plane, the zero-resistivity temperature rises from T_0 = 7.5K to 9K. **(c)** At T=2 K magnetic field was applied in plane (red) and out of plane (blue) to extract the upper critical fields H_{c2} for each direction, yielding an anisotropy term $\gamma \cong 2.1$.

V. Assessing the nonzero background resistance of Sample 1

Extensive resistivity measurements of sample 1 were made under different temperature, field and strain states. After mounting sample 1 on the strain device, a field, strain and temperature dependent background resistivity of order $\rho \approx 0.01\%$ was present, masking the true entrance into the zero-resistance state (Fig.S6). This may be due to a small volume of the sample which buckled under strain and thus behaves as if heavily-compressed, effectively raising its respective value of T_0 while still being highly strain, field and temperature dependent.

Here we describe the workaround to this issue. Prior to mounting on the strain device, the sample reached zero resistance at $T_0 = 7.5$ K. In Figure S6, the orange trace is under small tension ($\varepsilon_{xx} = 0.04\%$) and has a lower resistivity than the freestanding trace at all temperatures above T=9K, indicating an enhancement to the superconductivity. Below T=9 K, the orange trace has a higher resistivity and never reaches zero. The sample should be expected to reach zero resistance at higher temperature under tension, as is observed in sample 2. At T=7.5K, the orange trace should already be in a zero-resistance state, but instead has a value of approximately $\rho/\rho_0 = 1\%$. We thus use this value as a conservative estimate for the temperature and field entrance into the true zero resistance state. We determine the value of T_0 under fixed strain as $T_0(\varepsilon_{xx} = -.19\%) = 4$K, $T_0(\varepsilon_{xx} = .04\%) = 7.5$K, and $T_0(\varepsilon_{xx} = .20\%) = 10.3$K. We note that the data presented in Fig.S6 covers the full range of tensile and compressive strains we could apply with our device.

In Figure S7 we show the resistivity vs applied in-plane magnetic field data at several temperatures under $\varepsilon_{xx} = -.19\%$ (a) and $\varepsilon_{xx} = .20\%$ (b). The field values where the resistivity crosses $\rho/\rho_0 = 0.01\%$ are indicated by square markers, and these values are used to define the field-induced superconductivity phase space in the Main Text Figure 4.

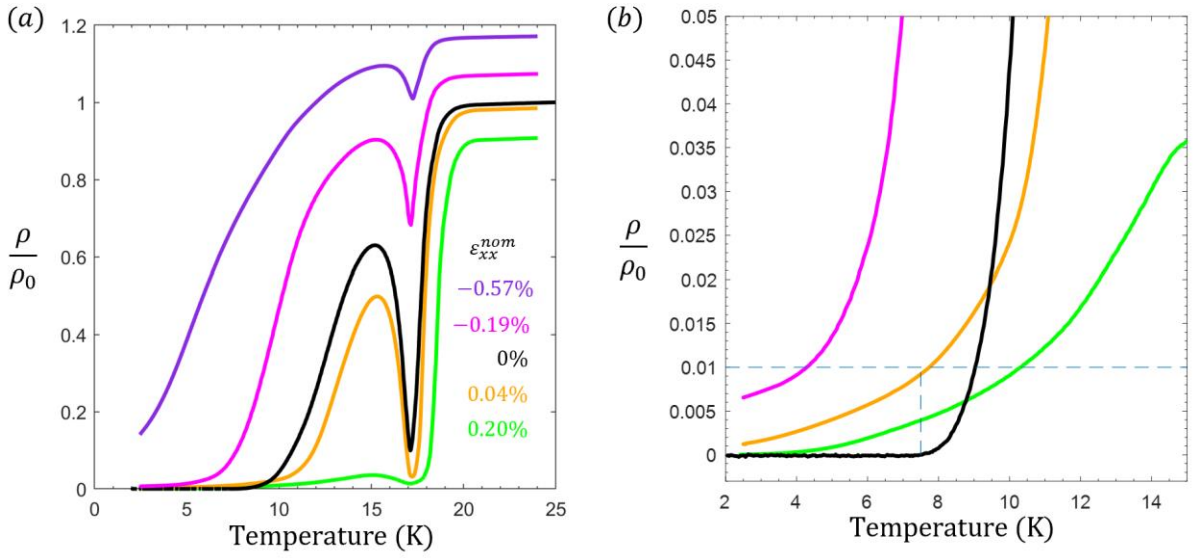

Figure S6. Strain-tuned superconducting transition.

(a) Sample 1. Resistivity vs temperature at two compressive and two tensile strain values, compared to freestanding value (black). **(b)** The same data zoomed to observe low resistivity values.

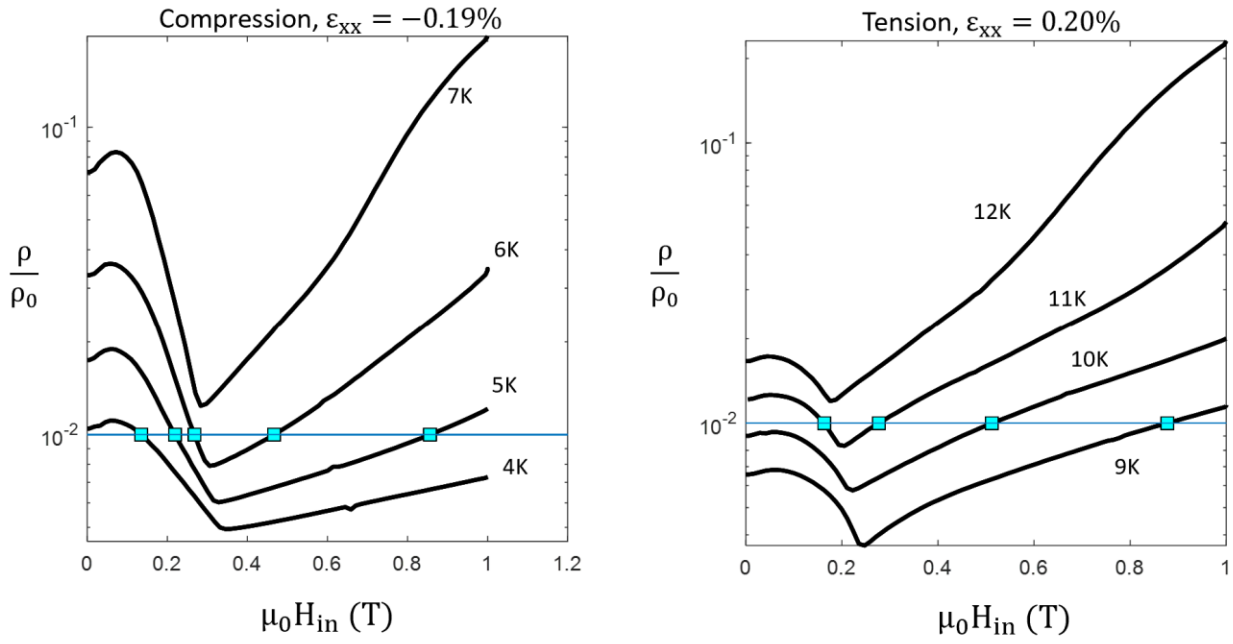

Figure S7. Small nonzero background resistivity.

Sample 1. Resistivity vs applied in-plane magnetic field under compression (left) and tension (right). The ρ/ρ_0>0.01 line marks the cutoff for estimated entrance into bulk zero-resistance state.

VI. Density Functional Theory Analysis of Eu-Fe exchange interactions

A puzzle is presented by the finding that an in-plane field is far more detrimental to superconductivity than an out of plane field above the Eu ferromagnetic ordering ($T_{SC} > T > T_{FM}$), while it promotes superconductivity below the maximum of the reentrant resistivity (Fig.S5). A plausible explanation can be given by considering the two competing effects of Eu moments on the Fe spin polarization. First, when Eu moments are aligned in-plane, the direct hybridization between Fe 3d states with Eu 4f states creates a spin-polarizing exchange bias, which pushes Eu-aligned Fe spin states at the Fermi surface up in energy and anti-aligned states down (Schrieffer-Wolfe interaction). This induces a direct exchange splitting $\Delta_d \sim t_{Fe(d)\text{-}Eu(f)}^2/(E_F\text{-}E_{Eu(f)})$, where the induced Fe polarization is *antiparallel* to that of the Eu ions. Second, there is a competing interaction due to hybridization between the Fe bands and the empty Eu d-bands. Since the latter are coupled to Eu 4f states though Hund rule's coupling, this effect leads to a net polarization of Fe that is *parallel* to Eu moments. A net polarization of Fe moments in *either* direction suppresses Cooper pairing.

In order to estimate these effects quantitatively, we have performed DFT calculations using the Wien2K package (*39*, *40*) to characterize these two effects. We find that both show high sensitivity to the Hubbard U on Eu sites, and as both are small and opposite in sign, their sum can be of either sign, or even of different signs in different bands. Below the Eu ferromagnetic transition, these two effects seem to largely cancel, and the dipole-field mechanism is dominant. Above the transition, the Eu moments do not fully saturate at small applied field, and the (accidental) cancelation between the two electronic effects will be lifted. This causes the itinerant Fe moments to gain a net magnetization for Eu moments aligned in-plane, which yields the stronger suppression of superconductivity with in-plane field. While we cannot calculate this exchange field with the required accuracy, given the strong dependence on the applied Hubbard correction, we can estimate the order of magnitude of the effect. We find that for fully in-plane polarized Eu moments (with $m = 7\ u_B$) and a variable U, the exchange interaction is within ±10 meV. This is far larger than the anticipated superconducting gap of the order of 2 meV (given T_{SC} = 19K), and so the scale of the effect – barring the above-discussed accidental cancellation – is on the right order to suppress superconductivity for the in-plane field. Meanwhile, for an out-of-plane applied field, Eu and Fe moments are perpendicular and the exchange splitting is only second order in the exchange field, resulting in a much weaker Eu-driven polarization of Fe spins and a far milder suppression of superconductivity. This explains why the effect of magnetic field shows the opposite anisotropy above and below the ferromagnetic ordering temperature of Eu.

Here we discuss the details of our calculations. We have used density functional theory (DFT) to characterize the effects of the Eu moments on the antiferromagnetically-ordered Fe moments via different exchange interactions, in order to estimate the band effects of Eu magnetism on Fe-origin superconductivity. We directly observe that both parallel and antiparallel Eu-Fe alignment effects are present, which appear to largely cancel out at low temperature.

We also show projected Fe d, Eu f and Eu d bands for κ=0 in Fig. S10. In the κ=0 case, Fe1 and Fe2 have equivalent small moments that have the same direction as the Eu moment, so we do not differentiate Fe1 and Fe2 in projected band. We can clearly see Fe d spin up bands pushed up above the Eu f bands, and this effect is larger closer to Eu f bands. Another effect is a non-negligible Fe d spin up contribution in the Eu f bands.

Comparing calculations with the full Hund's rule coupling (κ=1), where both Schrieffer-Wolfe Eu(f)-Fe(d) antiferromagnetic coupling and Hund's rule Eu(f)-Eu(d) ferromagnetic coupling is included, and those with κ=0, where only the former is operative, we see that (a) Eu(f)-Fe(d) is indeed antiferromagnetic (the red bands are always below the blue ones), and rather large for some bands at the Fermi level, while the competing Eu(f)-Eu(d) interactions is largely cancelling it for κ=1, and this cancellation is, fortuitously, nearly complete right at the Fermi level (while at ~0.2 eV below or above it becomes large, up to 100 meV). This confirms our conjecture of a fragile character of this cancellation.

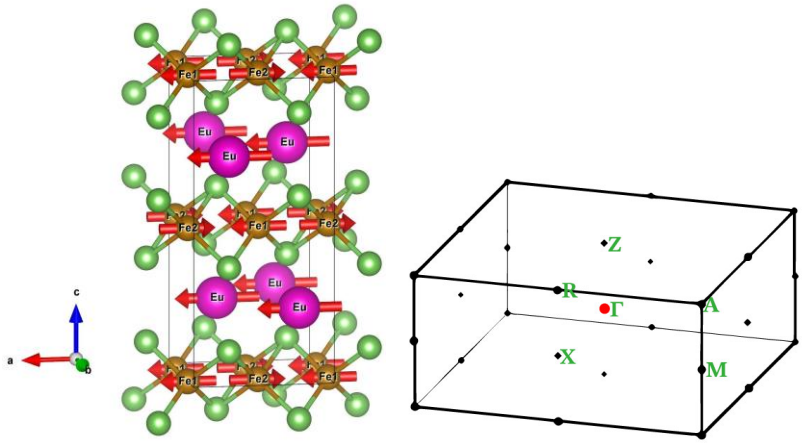

Figure S8. DFT calculations: Brillouin Zone.

Conventional structure, with *a* = 5.5372Å, *b* = 5.5052Å, *c* = 12.0572Å. Eu atoms are ferromagnetically ordered along the easy axis of the Fe antiferromagnetic order. High symmetry points of corresponding BZ are shown on right.

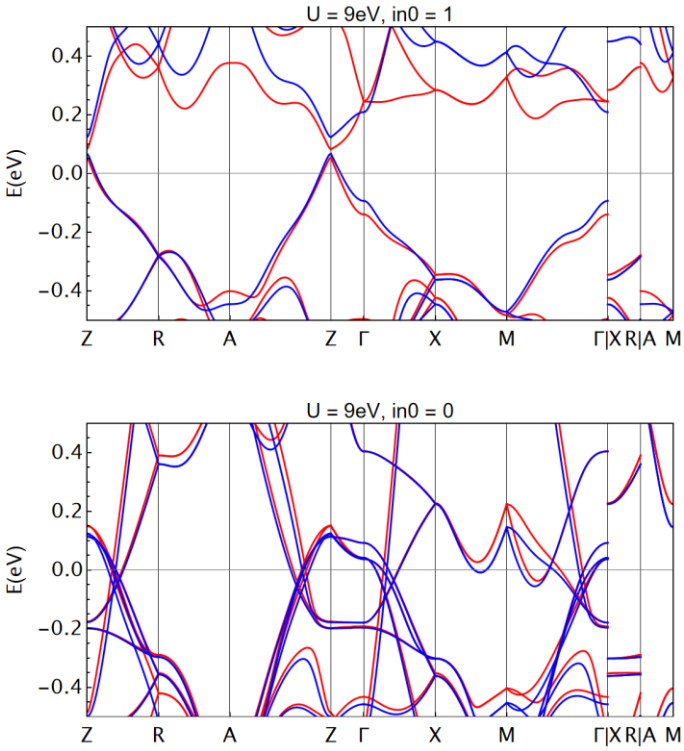

Figure S9. DFT calculations: Band Structure.

Band structure of U=9eV for κ=0 and 1. Red bands for spin up (aligned to Eu moments) and blue bands for spin down (anti-aligned to Eu moments).

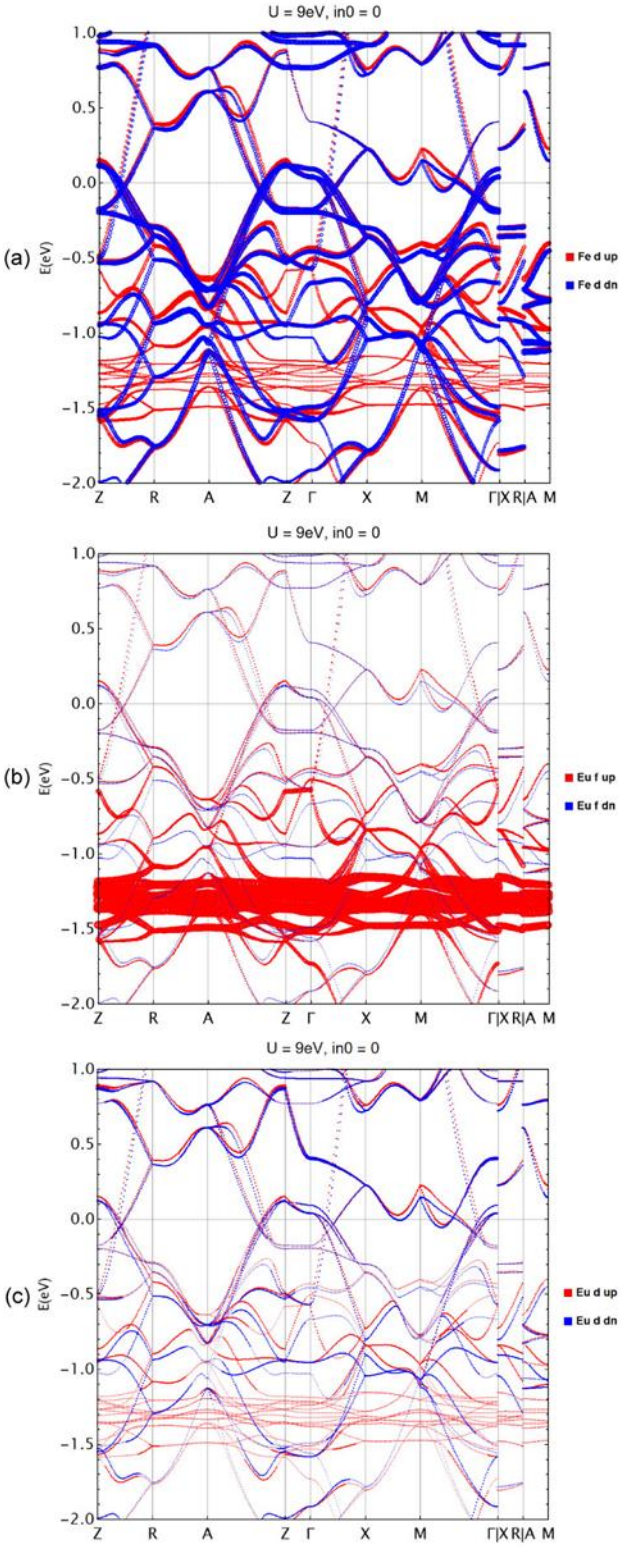

Figure S10. DFT calculations: Element-specific band structure.

Projected bands of (a) Fe d, (b) Eu f and (c) Eu d.

VII. Additional transport and XMCD data and details for Sample 2.

In the initial measurement of sample 2 in the x-ray compatible cryostat, zero resistance was obtained at zero applied magnetic field. During the measurement of the resistivity data in Fig.5E, it was noted that a small negative quadratic magnetoresistance background was present, causing the fully superconducting phase to appear to have negative resistance. We found that this was due to inductive noise from the wiring within the cryostat, which had not been optimized for low resistivity measurements. We fixed this wiring issue and reran the same sample under nearly-identical temperature, field and strain conditions to produce the data in Fig.5C,D, which did not show any negative magnetoresistance and which has not been corrected in any way. The data presented in Fig.5E was corrected to remove this background. To do so, we fit a quadratic function to the negative magnetoresistance of the sample in the highest-tension fully-superconducting state (Fig.S11, purple). This fit had an R^2 value of 0.97. The background had the most noticeable effect (<4%) at high field and only a very small effect (<0.5%) in the vicinity of 0.25T, where the minimum of the real sample magnetoresistance coincides with the full saturation of the Eu moments. Thus, we cannot say with certainty whether the +100V resistivity curve reaches zero resistance or not, while the analogous data in Fig.5C,D unambiguously does.

In Fig.S12, we present the complete set of (self-absorption corrected) x-ray absorption near-edge structure (XANES) and XMCD measurements performed in sample 2 used to produce Fig.5F. It is seen that strain does not visibly affect either quantity, confirming that strain has a minimal effect on the Eu magnetic order.

In Fig.S13, we present XMCD data at T=15K under large compression, and compare it to T=10K data at equivalent compression. Note that the XMCD self-absorption correction was not performed for the 15K data, as a necessary wide energy scan measurement was not performed at this temperature. To better compare it with the 10K data, we show here the 10K XMCD without the self-absorption correction, which is only subtly different from the version presented in Fig.S12.

In Fig.S14, we show resistivity vs device voltage at T=7K, below the zero-strain superconducting zero-resistance temperature, at both zero field and at the optimal in-plane field of 0.26T. We compare this with the main text figure 5C, which is an equivalent data set at T=10K. At T=7K, zero resistance is found over a wide strain range.

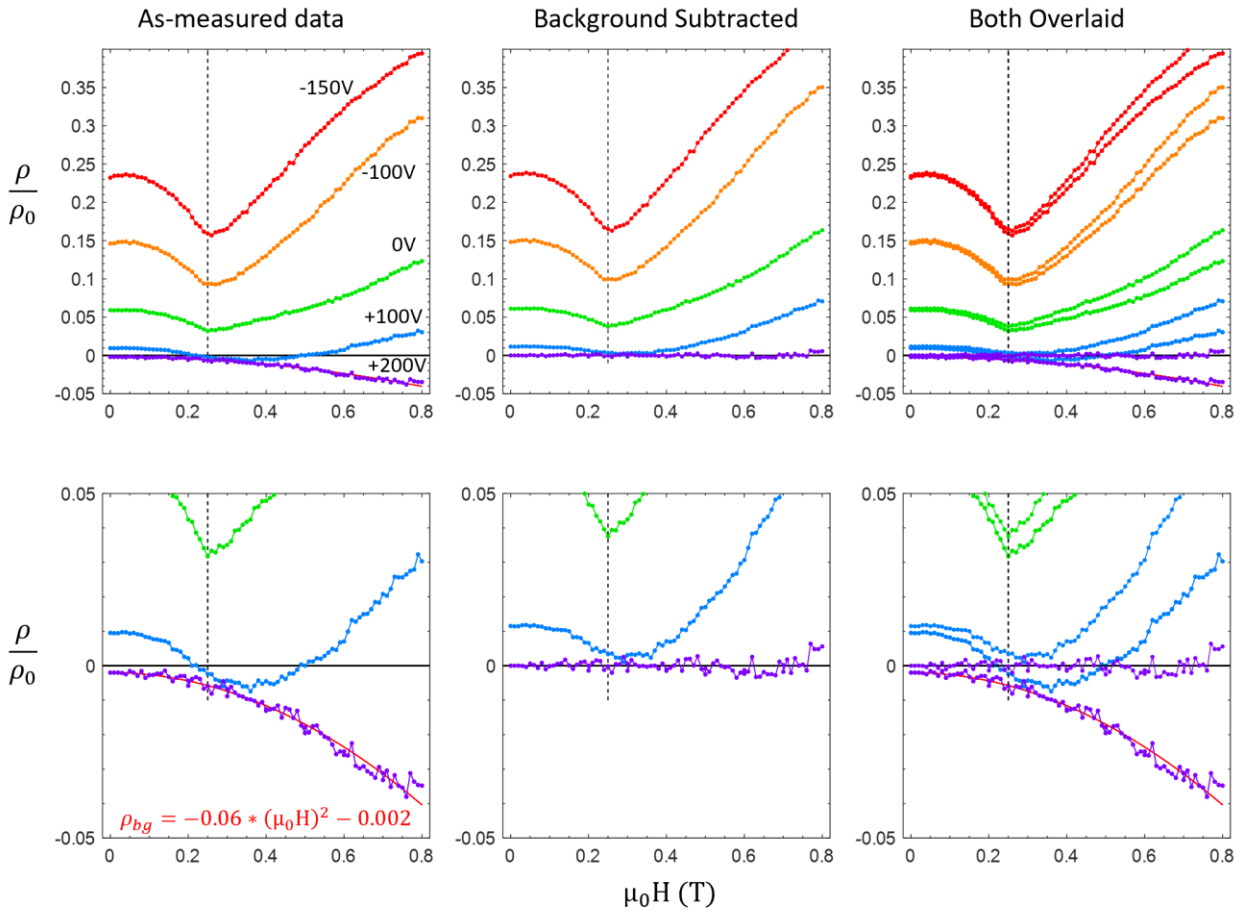

Figure S11. Field-dependent magnetoresistance background subtraction.

Resistivity vs field for data in main text Fig.5E. Bottom plots are zoomed in to small resistance range. Negative quadratic magnetoresistance (red fit line) present as a background signal during the data collection. This background was subtracted from all 5 resistivity traces. The overlay of pre- and post-background subtracted data shows that this background has a minimal effect on the resistivity near 0.25T. Thus, it is clear that the minimum of the magnetoresistance corresponds to the full in-plane polarization of Eu moments.

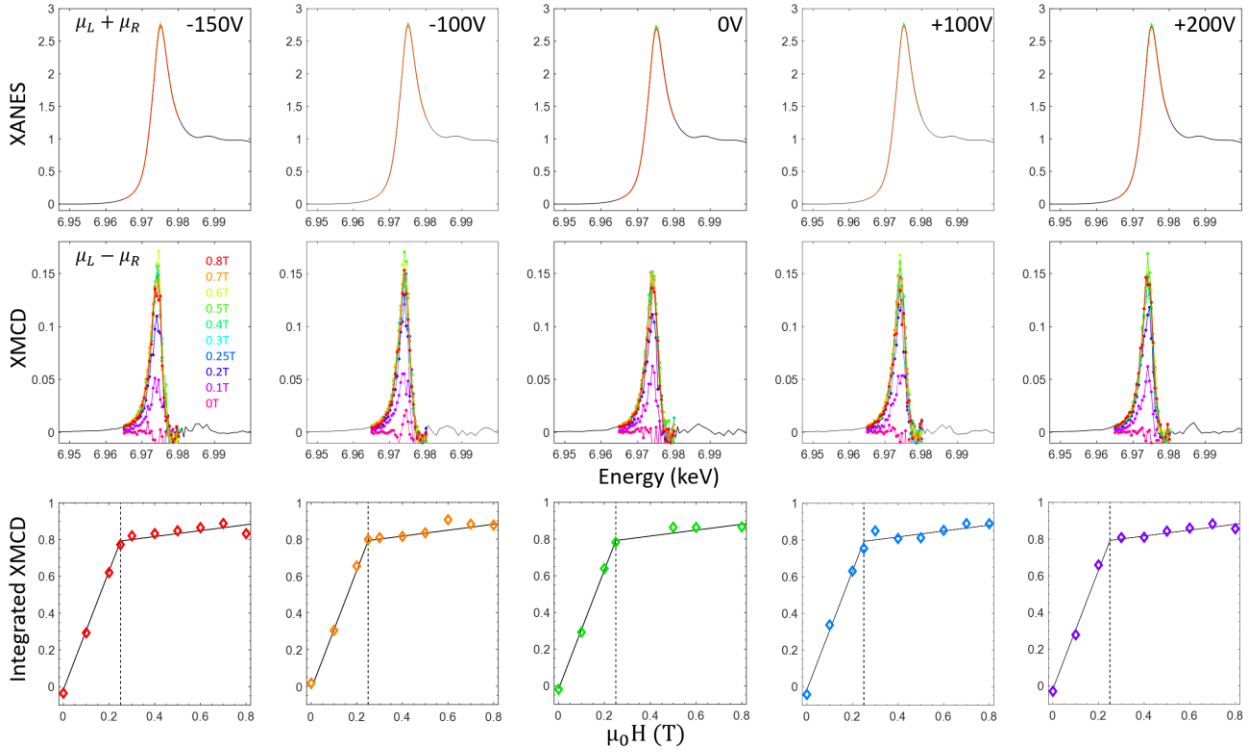

Figure S12. XMCD full spectra.

Sample 2. X-ray spectroscopy under strain and field at T=10K from main text Fig.5F. μ_L and μ_R refer to left and right circular polarized light. Top: X-ray absorption near edge spectrum (XANES). Middle: X-ray magnetic circular dichroism (XMCD). Bottom: sum of the XMCD data, normalized to the T=2K XMCD signal (see Fig.S4). Lines are a guide to the eye and are the same in all figures. Black traces in top/middle are wider energy scans at 0.8T applied field. Colored scans are narrow energy scans at field values 0-0.8T. Bottom plots are color coded as in Fig.5F. Left to right is strain from compression to tension. The field-tuned XANES are superimposed in top figures and are nearly indistinguishable. Further, strain tuning has virtually no effect on the XANES. The XMCD figures change only subtly with strain at same equal field values.

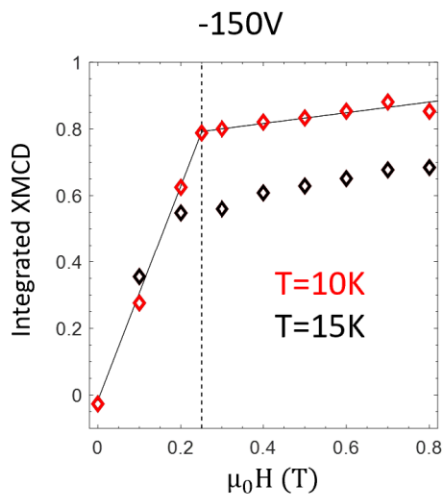

Figure S13. XMCD at 10K and 15K.

Sample 2. XMCD vs field at 15K and 10K under large compression (-150V). The Eu magnetic moment at 15K is clearly reduced relative to 10K, and correspondingly reaches saturation at a lower field.

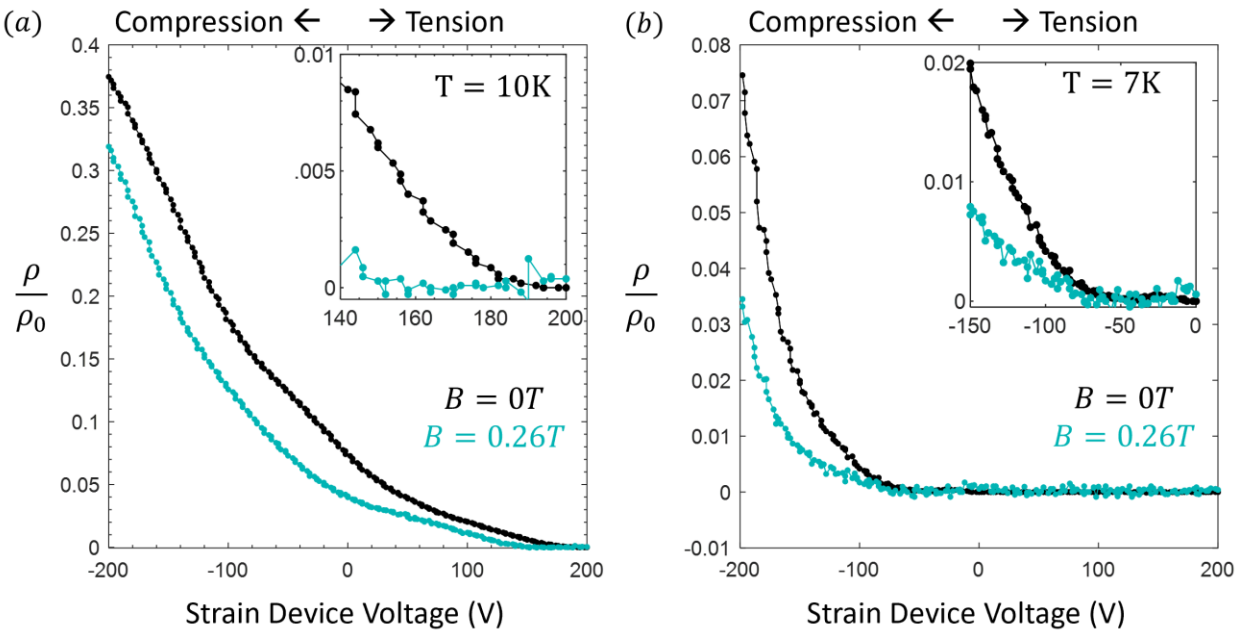

Figure S14. Strain and field tunable resistivity above and below the zero-resistance temperature.

Sample 2. Resistivity vs strain device voltage at (a) T=10K and (b) T=7K. Note that at T=10K, tension must be applied to induce zero resistance, while at T=7K, compression must be applied to return to a nonzero resistance state. In both cases, a near-optimal applied magnetic field reduces the resistivity at all voltages.

REFERENCES AND NOTES

1. D. N. Basov, R. D. Averitt, D. Hsieh, Towards properties on demand in quantum materials. *Nat. Mater.* **16**, 1077–1088 (2017).

2. S. Nandi, W. T. Jin, Y. Xiao, Y. Su, S. Price, D. K. Shukla, J. Strempfer, H. S. Jeevan, P. Gegenwart, Th. Brückel, Coexistence of superconductivity and ferromagnetism in P-doped $EuFe_2As_2$. *Phys. Rev. B* **89**, 014512 (2014).

3. W.-H. Jiao, Q. Tao, Z. Ren, Y. Liu, G.-H. Cao, Evidence of spontaneous vortex ground state in an iron-based ferromagnetic superconductor. *npj Quantum Mater.* **2**, 50 (2017).

4. V. S. Stolyarov, I. S. Veshchunov, S. Yu. Grebenchuk, D. S. Baranov, I. A. Golovchanskiy, A. G. Shishkin, N. Zhou, Z. Shi, X. Xu, S. Pyon, Y. Sun, W. Jiao, G.-H. Cao, L. Ya. Vinnikov, A. A. Golubov, T. Tamegai, A. I. Buzdin, D. Roditchev, Domain Meissner state and spontaneous vortex-antivortex generation in the ferromagnetic superconductor $EuFe_2(As_{0.79}P_{0.21})_2$. *Sci. Adv.* **4**, eaat1061 (2018).

5. J. Linder, J. W. A. Robinson, Superconducting spintronics. *Nat. Phys.* **11**, 307–315 (2015).

6. G. D. Simoni, E. Strambini, J. S. Moodera, F. S. Bergeret, F. Giazotto, Toward the absolute spin-valve effect in superconducting tunnel junctions. *Nano Lett.* **18**, 6369–6374 (2018).

7. M. G. Flokstra, N. Satchell, J. Kim, G. Burnell, P. J. Curran, S. J. Bending, J. F. K. Cooper, C. J. Kinane, S. Langridge, A. Isidori, N. Pugach, M. Eschrig, H. Luetkens, A. Suter, T. Prokscha, S. L. Lee, Remotely induced magnetism in a normal metal using a superconducting spin-valve. *Nat. Phys.* **12**, 57–61 (2016).

8. B. Li, N. Roschewsky, B. A. Assaf, M. Eich, M. Epstein-Martin, D. Heiman, M. Münzenberg, J. S. Moodera, Superconducting spin switch with infinite magnetoresistance induced by an internal exchange field. *Phys. Rev. Lett.* **110**, 097001 (2013).

9. H. W. Meul, C. Rossel, M. Decroux, Ø. Fischer, G. Remenyi, A. Briggs, Observation of magnetic-field-induced superconductivity. *Phys. Rev. Lett.* **53**, 497–500 (1984).

10. J. Cors, R. Baíllif, M. G. Karkut, M. Decroux, Ø. Fischer, U. Welp, G. Bruls, Observation of magnetic-field-induced superconductivity in Se-doped EuMo6S8 under pressure. *Europhys. Lett.* **3**, 635–641 (1987).

11. F. Lévy, I. Sheikin, B. Grenier, A. D. Huxley, Magnetic field-induced superconductivity in the ferromagnet URhGe. *Science* **309**, 1343–1346 (2005).

12. P. T. Yang, Z. Y. Liu, K. Y. Chen, X. L. Liu, X. Zhang, Z. H. Yu, H. Zhang, J. P. Sun, Y. Uwatoko, X. L. Dong, K. Jiang, J. P. Hu, Y. F. Guo, B. S. Wang, J.-G. Cheng, Pressured-induced superconducting phase with large upper critical field and concomitant enhancement of antiferromagnetic transition in $EuTe_2$. *Nat. Commun.* **13**, 2975 (2022).

13. G. Knebel, W. Knafo, A. Pourret, Q. Niu, M. Vališka, D. Braithwaite, G. Lapertot, M. Nardone, A. Zitouni, S. Mishra, I. Sheikin, G. Seyfarth, J.-P. Brison, D. Aoki, J. Flouquet, Field-reentrant superconductivity close to a metamagnetic transition in the heavy-fermion superconductor UTe_2. *J. Physical Soc. Japan* **88**, 063707 (2019).

14. S. Ran, S. R. Saha, I. L. Liu, D. Graf, J. Paglione, N. P. Butch, Expansion of the high field-boosted superconductivity in UTe_2 under pressure. *npj Quantum Mater.* **6**, 75 (2021).

15. T. Konoike, S. Uji, T. Terashima, M. Nishimura, S. Yasuzuka, K. Enomoto, H. Fujiwara, B. Zhang, H. Kobayashi, Magnetic-field-induced superconductivity in the antiferromagnetic organic superconductor κ−$(BETS)_2FeBr_4$. *Phys. Rev. B* **70**, 094514 (2004).

16. K. Hiraki, H. Mayaffre, M. Horvatić, C. Berthier, S. Uji, T. Yamaguchi, H. Tanaka, A. Kobayashi, H. Kobayashi, T. Takahashi, ^{77}Se NMR evidence for the jaccarino–Peter mechanism in the field induced superconductor, λ-$(BETS)_2FeCl_4$. *J. Physical Soc. Japan* **76**, 124708 (2007).

17. S. Jiang, H. Xing, G. Xuan, Z. Ren, C. Wang, Z. Xu, G. Cao, Superconductivity and local-moment magnetism in $Eu(Fe_{0.89}Co_{0.11})_2As_2$. *Phys. Rev. B* **80**, 184514 (2009).

18. U. B. Paramanik, P. L. Paulose, S. Ramakrishnan, A. K. Nigam, C. Geibel, Z. Hossain, Magnetic and superconducting properties of Ir-doped $EuFe_2As_2$. *Supercond. Sci. Technol.* **27**, 075012 (2014).

19. W.-H. Jiao, H.-F. Zhai, J.-K. Bao, Y.-K. Luo, Q. Tao, C.-M. Feng, Z.-A. Xu, G.-H. Cao, Anomalous critical fields and the absence of Meissner state in $Eu(Fe_{0.88}Ir_{0.12})_2As_2$ crystals. *New J. Phys.* **15**, 113002 (2013).

20. H. S. Jeevan, D. Kasinathan, H. Rosner, P. Gegenwart, Interplay of antiferromagnetism, ferromagnetism, and superconductivity in $EuFe_2(As_{1-x}P_x)_2$ single crystals. *Phys. Rev. B.* **83**, 054511 (2011).

21. S. Zapf, M. Dressel, Europium-based iron pnictides: A unique laboratory for magnetism, superconductivity and structural effects. *Rep. Prog. Phys.* **80**, 016501 (2017).

22. A. Baumgartner, D. Neubauer, S. Zapf, A. V. Pronin, W. H. Jiao, G. H. Cao, M. Dressel, Reentrant phases in electron-doped $EuFe_2As_2$: Spin glass and superconductivity. *Phys. Rev. B* **95**, 174522 (2017).

23. I. Nowik, I. Felner, Z. Ren, G. H. Cao, Z. A. Xu, Coexistence of ferromagnetism and superconductivity: Magnetization and Mössbauer studies of $EuFe_2(As_{1-x}P_x)_2$. *J. Phys. Condens. Matter* **23**, 065701 (2011).

24. W.-H. Jiao, J.-K. Bao, Q. Tao, H. Jiang, C.-M. Feng, Z.-A. Xu, G.-H. Cao, Evolution of superconductivity and ferromagnetism in $Eu(Fe_{1-x}Ru_x)_2As_2$. *J. Phys. Conf. Ser.* **400**, 022038 (2012).

25. W. T. Jin, Y. Xiao, Z. Bukowski, Y. Su, S. Nandi, A. P. Sazonov, M. Meven, O. Zaharko, S. Demirdis, K. Nemkovski, K. Schmalzl, L. M. Tran, Z. Guguchia, E. Feng, Z. Fu, Th. Brückel, Phase diagram of Eu magnetic ordering in Sn-flux-grown $Eu(Fe1{-}xCox)_2As_2$ single crystals. *Phys. Rev. B* **94**, 184513 (2016).

26. W. T. Jin, W. Li, Y. Su, S. Nandi, Y. Xiao, W. H. Jiao, M. Meven, A. P. Sazonov, E. Feng, Y. Chen, C. S. Ting, G. H. Cao, Th. Brückel, Magnetic ground state of superconducting $Eu(Fe_{0.88}Ir_{0.12})_2As_2$: A combined neutron diffraction and first-principles calculation study. *Phys. Rev. B* **91**, 064506 (2015).

27. V. H. Tran, T. A. Zaleski, Z. Bukowski, L. M. Tran, A. J. Zaleski, Tuning superconductivity in $Eu(Fe_{0.81}Co_{0.19})_2As_2$ with magnetic fields. *Phys. Rev. B* **85**, 052502 (2012).

28. A. Löhle, A. Baumgartner, S. Zapf, M. Dressel, W. H. Jiao, G. H. Cao, Effects of pressure and magnetic field on the reentrant superconductor $Eu(Fe_{0.93}Rh_{0.07})_2As_2$. *Phys. Rev. B.* **95**, 195146 (2017).

29. M. S. Ikeda, T. Worasaran, J. C. Palmstrom, J. A. W. Straquadine, P. Walmsley, I. R. Fisher, Symmetric and antisymmetric strain as continuous tuning parameters for electronic nematic order. *Phys. Rev. B* **98**, 245133 (2018).

30. P. Malinowski, Q. Jiang, J. J. Sanchez, J. Mutch, Z. Liu, P. Went, J. Liu, P. J. Ryan, J.-W. Kim, J.-H. Chu, Suppression of superconductivity by anisotropic strain near a nematic quantum critical point. *Nat. Phys.* **16**, 1189–1193 (2020).

31. J. J. Sanchez, P. Malinowski, J. Mutch, J. Liu, J.-W. Kim, P. J. Ryan, J.-H. Chu, The transport–Structural correspondence across the nematic phase transition probed by elasto X-ray diffraction. *Nat. Mater.* **20**, 1519–1524 (2021).

32. X. Chen, S. Maiti, R. M. Fernandes, P. J. Hirschfeld, Nematicity and superconductivity: Competition versus cooperation. *Phys. Rev. B* **102**, 184512 (2020).

33. A. Akbari, P. Thalmeier, I. Eremin, Evolution of the multiband Ruderman–Kittel–Kasuya–Yosida interaction: Application to iron pnictides and chalcogenides. *New J. Phys.* **15**, 033034 (2013).

34. J. J. Sanchez, G. Fabbris, Y. Choi, Y. Shi, P. Malinowski, S. Pandey, J. Liu, I. I. Mazin, J.-W. Kim, P. Ryan, J.-H. Chu, Strongly anisotropic antiferromagnetic coupling in $EuFe_2As_2$ revealed by stress detwinning. *Phys. Rev. B* **104**, 104413 (2021).

35. S. Zapf, C. Stingl, K. W. Post, J. Maiwald, N. Bach, I. Pietsch, D. Neubauer, A. Löhle, C. Clauss, S. Jiang, H. S. Jeevan, D. N. Basov, P. Gegenwart, M. Dressel, Persistent detwinning of iron-pnictide $EuFe_2As_2$ crystals by small external magnetic fields. *Phys. Rev. Lett.* **113**, 227001 (2014).

36. J. Maiwald, I. I. Mazin, P. Gegenwart, Microscopic theory of magnetic detwinning in iron-based superconductors with large-spin rare earths. *Phys. Rev. X* **8**, 011011 (2018).

37. V. Jaccarino, M. Peter, Ultra-high-field superconductivity. *Phys. Rev. Lett.* **9**, 290–292 (1962).

38. L. Balicas, J. S. Brooks, K. Storr, S. Uji, M. Tokumoto, H. Tanaka, H. Kobayashi, A. Kobayashi, V. Barzykin, L. P. Gor'kov, Superconductivity in an organic insulator at very high magnetic fields. *Phys. Rev. Lett.* **87**, 067002 (2001).

39. P. Blaha, K. Schwarz, F. Tran, R. Laskowski, G. K. H. Madsen, L. D. Marks, WIEN2k: An APW+lo program for calculating the properties of solids. *J. Chem. Phys.* **152**, 074101 (2020).

40. J. P. Perdew, K. Burke, M. Ernzerhof, Generalized gradient approximation made simple. *Phys. Rev. Lett.* **77**, 3865–3868 (1996).

41. I. Nowik, I. Felner, Z. Ren, G. H. Cao, Z. A. Xu, ^{57}Fe and ^{151}Eu Mössbauer spectroscopy and magnetization studies of $Eu(Fe_{0.89}Co_{0.11})_2As_2$ and $Eu(Fe_{0.9}Ni_{0.1})_2As_2$. *New J. Phys.* **13**, 023033 (2011).

42. H. S. Jeevan, Z. Hossain, D. Kasinathan, H. Rosner, C. Geibel, P. Gegenwart, Electrical resistivity and specific heat of single-crystalline $EuFe_2As_2$: A magnetic homologue of $SrFe_2As_2$. *Phys. Rev. B* **78**, 052502 (2008).

43. A. Pogrebna, T. Mertelj, N. Vujičić, G. Cao, Z. A. Xu, D. Mihailovic, Coexistence of ferromagnetism and superconductivity in iron based pnictides: A time resolved magnetooptical study. *Sci. Rep.* **5**, 7754 (2015).

44. V. L. Ginzburg, Ferromagnetic superconductors. *Soviet Physics–JETP* **4**, 153 (1956).

45. Zh. Devizorova, S. Mironov, A. Buzdin, Theory of magnetic domain phases in ferromagnetic superconductors. *Phys. Rev. Lett.* **122**, 117002 (2019).

46. M. Kano, Y. Kohama, D. Graf, F. Balakirev, A. S. Sefat, M. A. Mcguire, B. C. Sales, D. Mandrus, S. W. Tozer, Anisotropy of the upper critical field in a co-doped $BaFe_2As_2$ single crystal. *J. Physical Soc. Japan* **78**, 084719 (2009).

47. N. Ni, M. E. Tillman, J.-Q. Yan, A. Kracher, S. T. Hannahs, S. L. Bud'ko, P. C. Canfield, Effects of Co substitution on thermodynamic and transport properties and anisotropic H_{c2} in $Ba(Fe_{1-x}Co_x)_2As_2$ single crystals. *Phys. Rev. B* **78**, 214515 (2008).

48. M. Hemmida, N. Winterhalter-Stocker, D. Ehlers, H.-A. K. von Nidda, M. Yao, J. Bannies, E. D. L. Rienks, R. Kurleto, C. Felser, B. Büchner, J. Fink, S. Gorol, T. Förster, S. Arsenijevic, V. Fritsch, P. Gegenwart, Topological magnetic order and superconductivity in $EuRbFe_4As_4$. *Phys. Rev. B* **103**, 195112 (2021).

49. X. Xi, Z. Wang, W. Zhao, J.-H. Park, K. T. Law, H. Berger, L. Forró, J. Shan, K. F. Mak, Ising pairing in superconducting $NbSe_2$ atomic layers. *Nat. Phys.* **12**, 139–143 (2016).

50. J. M. Lu, O. Zheliuk, I. Leermakers, N. F. Q. Yuan, U. Zeitler, K. T. Law, J. T. Ye, Evidence for two-dimensional Ising superconductivity in gated MoS_2. *Science* **350**, 1353–1357 (2015).

51. W. Fang, K. D. Belashchenko, M. Haim, M. Khodas, I. I. Mazin, Interplay of magnetic field and magnetic impurities in Ising superconductors. arXiv: 2306.01700 [cond-mat.supr-con] (2 June 2023).

52. E. G. Arnault, A. H. Al-Tawhid, S. Salmani-Rezaie, D. A. Muller, D. P. Kumah, M. S. Bahramy, G. Finkelstein, K. Ahadi, Anisotropic superconductivity at $KTaO_3$(111) interfaces. *Sci. Adv.* **9**, eadf1414 (2023).

53. D. Jiang, T. Yuan, Y. Wu, X. Wei, G. Mu, Z. An, W. Li, Strong In-plane magnetic field-induced reemergent superconductivity in the van der waals heterointerface of $NbSe_2$ and $CrCl_3$. *ACS Appl. Mater. Interfaces* **12**, 49252–49257 (2020).

54. H. Zhao, R. Blackwell, M. Thinel, T. Handa, S. Ishida, X. Zhu, A. Iyo, H. Eisaki, A. N. Pasupathy, K. Fujita, Smectic pair-density-wave order in $EuRbFe_4As_4$. *Nature* **618**, 940–945 (2023).

55. A. A. Bukharaev, A. K. Zvezdin, A. P. Pyatakov, Y. K. Fetisov, Straintronics: A new trend in micro- and nanoelectronics and materials science. *Phys. Usp.* **61**, 1175–1212 (2018).

56. R. Prozorov, M. A. Tanatar, N. Ni, A. Kreyssig, S. Nandi, S. L. Bud'ko, A. I. Goldman, P. C. Canfield, Intrinsic pinning on structural domains in underdoped single crystals of $Ba(Fe_{1-x}Cox)_2As_2$. *Phys. Rev. B* **80**, 174517 (2009).

57. G. Wang, W. R. Meier, W. E. Straszheim, J. Slagle, S. L. Bud'ko, P. C. Canfield, Lack of superconductivity in the phase diagram of single-crystalline $Eu(Fe_{1-x}Co_x)_2As_2$ grown by transition metal arsenide flux. *Phys. Rev. Mater.* **2**, 104801 (2018).

-